Title

Structural modification of oxazolidinone antibiotics alters nascent peptide stalling preference and peptide trajectory through the ribosome

ISBN

9798189299452

Author

Kleinman, Jordan Isabelle

Publication Date

2026-09-03

Peer reviewed|Thesis/dissertation

Structural modification of oxazolidinone antibiotics alters nascent peptide stalling preference and peptide trajectory through the ribosome

by

Jordan Isabelle Kleinman

DISSERTATION

Submitted in partial satisfaction of the requirements for degree of

DOCTOR OF PHILOSOPHY

in

Chemistry and Chemical Biology

in the

GRADUATE DIVISION

of the

UNIVERSITY OF CALIFORNIA, SAN FRANCISCO

Approved:

DocuSigned by:
Danica Galonic Fujimori
82967A5AE18B4D6...

Danica Galonic Fujimori

Chair

Signed by:
John D Gross
DocuSigned by:
Davide Ruggero
14C3B6AD60C5446...

John D Gross

Davide Ruggero

Committee Members

Dedication

This PhD has been a long, LONG time coming, and I couldn't have made it through without my amazing support network of family and friends. You all have kept me (reasonably) (semi) sane through the chaos, encouraged me when I was down, provided much-needed distractions and talked me off ledges when the science wasn't working, and brought so much silliness and joy into my life. I love you all!!!

First, I want to say thank you to my whole obnoxious family. My parents, grandparents, siblings, aunts, uncles, and cousins, who are constantly asking for timeline updates and being excited with me when things are going well, even if the details are sometimes a bit of a blur. All of your support and care packages and gargantuan family gatherings along the way have kept me going to reach this point. I am very excited to finally be able to give you a resolution on #FreeJordan!

Mom – Thank you for always being there to listen to me vent and to encourage me and provide delicious foods and cute crafts. Our nightly video chats have been a bright spot when I'm feeling down, and I love hearing about all your fun (and impressive!) projects and yoga exploits. Thank you for convincing me that I'm capable even when I feel like I'm drowning.

Dad – You're one of my favorite people to go to when I have a problem, because you help me talk things through and always have at least one suggestion or solution to hand. I love that we share similar interests and can trade book recs for when I want to talk science fiction instead of science, but that I can also talk to you about what I'm doing in lab. Thank you for all

your (delightfully) terrible jokes and silly faces and always being up for a game to take my mind off of it!

Mama and Papa – I have spent so much time over this PhD stressing, but our massive family gatherings and vacations are always something wonderful to look forward to on the horizon. Thank you for getting us all together and facilitating the crazy! I really appreciate your check-ins and carrying pickles all the way across SF just because I made an off-hand request. The ribosomes have asked me to tell you that they're good and they say hi!

Grandma Elaine and Grandpa Mickey – Thank you for being so supportive of me all these years! It means so much to pick up the phone and be told it's just because you want to hear my voice, and I'm sorry I don't manage to call more. Grandpa Mickey, it's been especially helpful to be able to get your perspective on my work and on the PhD from the other side, and I always enjoy hearing more about your research as well!

My goofy Aunt Sheryl – thank you for all of the care packages and lunches and always having something to say to brighten my day!

Andrew, Dani, and Jessa – Even though none of us is all that great at communicating when we're apart, our random silly text exchanges or phone calls never fail to make me smile. Thank you for being so (awesomely) easy to tease, it always helps me to feel better :P

Second, a thank you to all of my wonderful friends, from grad school and beyond. It would be impossible to mention all of you and all of the wonderful times we have had, but I love you all more than I can say for being there for me! Whether it's by going for a hike or karaoke or dinner, letting me talk your ear off at lunch, inviting me for a last minute craft night, listening to

the umpteenth iteration of problems with a particularly troublesome experiment, or just putting up with me vanishing for extended periods of time and then picking back up when the stress cools, your friendship has truly kept me afloat and functioning as a human being.

Regan – I beyond grateful to have gotten to know you from before even the official start of our program, living in a sketchy hotel til the student housing was finished – I couldn't have asked for a better friend to go through the tumult of grad school with. Thank you for being so codependent with me, because I would be a million times less brave without you. I love living close enough that I can just pop over for a random movie night or cat therapy or just to chat, and I truly don't know what I'll do if we end up getting jobs in different places.

Dyana and Maddie – I am so lucky that Dyana decided to be a bootcamp coordinator during my first year, because it's meant that I get to know the two of you. It's always such a relief knowing we have a movie night to look forward to during the week, because after all the venting is done, being able to go brain off and eat way too much cheese and discuss silly topics (and do a crossword) with good friends is such a needed balm. Thank you also for listening to far more iterations of my research presentation than anyone should ever have to, and for encouraging me to try lots of fun new things!

Alicia – I miss you so much being so far away, but it is so amazing to see you living out your dreams and moving to the UK for graduate school! I'm continually impressed at your bravery, and at your insane cooking exploits, and I love hearing about all your adventures – I'm so glad to see you thriving! I am beyond lucky to have such a wonderful friend who understands when I go radio silent, and to be totally ready to pick right back up where we left off when I emerge from the abyss. I love you!

David, Katie, and Jeffrey – Thank you for all the floor time and impromptu dinner parties, and for the company during stupid late nights in lab, when we really should have left forever ago but are having far too much fun procrastinating and crafting and being silly together. I love being able to walk in and identify each of your distinctive laughter from all the way down the hall, and I'm really going to miss seeing you every day. We may not be able to lock in when we're all together, but you've provided so much direct love and support and feedback throughout the process of writing the paper and this dissertation especially, and I would probably be setting a world record on PhD length if I had to do it without you.

Fujimori Lab Crew – I couldn't have asked for a better, more friendly, or more collaborative lab experience and that is all thanks to you. It's wonderful to be able to look forward to going into work even if the science is stalled, because it means I have so many friends to commiserate with and bounce ideas off of until we get it working again – and when it is working, to share in the excited speculation and experiment planning! Our switch nights and many food- or movie-centric outings are a blast, and I'm so glad that we continue to make the time for them even after many have graduated and even if they are more sporadic. I appreciate that we're constantly learning from one another (whether about science or about wild drama in the wrestling world) and that I know I can always depend on you when I need a hand.

Finally, a massive thank you to Danica, without whom none of this work would have been possible. I initially decided to come to UCSF after a phone call from you welcoming me to the program where you let me ask a million and one questions, and I am so glad that I did. Thank you so much for welcoming me into your lab, offering me such an interesting research topic, and building such a wonderful lab environment in which to learn and grow. Your mentorship has been invaluable over the years, and I am certainly a better scientist and presenter for it.

Acknowledgements

We thank D. Bulkley and G. Gilbert for technical support at the UCSF Center for Advanced CryoEM, which is supported by the National Institutes of Health (S10OD020054, S10OD021741, and S10OD026881) and the Howard Hughes Medical Institute (HHMI). Sequencing was performed at the UCSF CAT, supported by UCSF PBBR, RRP IMIA, and NIH 1S10OD028511-01 grants. We acknowledge support from NIAID (R01AI137270 to D.G.F. and F31AI181568 to J.I.K.), NIGMS (R35GM145238 to J.S.F and R35GM127134 to A.S.M.), and W.M. Keck Foundation Medical Research Grant (to J.S.F. and D.G.F.).

Contributions

Data presented in this dissertation are adapted from unpublished work that has been submitted for publication:

Kleinman, JI; Raskar, T; Klepacki, D; Szal, T; Vázquez-Laslop, N; Mankin, AS; Fraser, JS; Fujimori, DG. Structural modification of oxazolidinone antibiotics alters nascent peptide stalling preference and peptide trajectory through the ribosome. bioRxiv 2026 *(under revision with Nature Chemical Biology)*. doi: 10.64898/2026.02.16.706219

Experiments for revisions to this manuscript for publication were completed by Jordan Kleinman and Adam Oken.

Data Availability:

Atomic coordinates and cryo-EM density maps for all the structures presented here have been deposited in the Protein Data Bank and Electron Microscopy Data Bank (EMDB) with the following accession numbers: 10ZD and EMD-75563 (TZD-MNTAIK-SRC), 10ZE and EMD-75564 (MNTAIK-only RNC), 37DY and EMD-78106 (DZD-MNTAIK SRC), 37EA and EMD-78108 (TZD-MYVRHE SRC), 37DZ and EMD-78107 (DZD-MYVRHE SRC), and 37DX and EMD-78105 (MYVRHE-only RNC). The following datasets were used to generate the initial volumes for the presented structures: wild-type *Escherichia coli* stalled ribosome with antibiotic linezolid, PDB ID 7S1G. Raw and processed sequencing data were deposited in the GEO database under SuperSeries accession number GSE319740. Processing and analysis scripts for sequencing data are available at github.com/jikleinman/RiboSeq-Code.

Structural modification of oxazolidinone antibiotics alters nascent peptide stalling preference and peptide trajectory through the ribosome

Jordan Isabelle Kleinman

Abstract

The oxazolidinone antibiotic linezolid binds to the peptidyl transferase center of the ribosome, where it inhibits a subset of peptide bond formation events. This context-specificity of translation inhibition is dictated by the nature of the amino acid at the penultimate position of the nascent peptide. It remains unknown whether this is a general feature of oxazolidinones and whether it can be modulated by their structural alterations. Here, we show that the oxazolidinone tedizolid also inhibits translation in a context-specific manner, but with dramatically altered selectivity, favoring Ile, His, and Gln as the penultimate (-1) residues. Delpazolid, which shares the C5-hydroxymethyl moiety with tedizolid, shows a similar preference. Structural analysis of ribosomes stalled by tedizolid or delpazolid revealed differences in nascent peptide conformation as a function of the penultimate amino acid, with Ile(-1) peptide adopting a compacted, helical conformation induced by the drug, while His(-1) peptides favored a more extended conformation, facilitated by extensive interactions of the imidazole moiety with both rRNA and the oxazolidinone ligand. Our findings reveal that stalling preferences of oxazolidinones can be modulated by structural modifications of antibiotic scaffold and conformational malleability of the nascent chain.

Table of Contents

List of Figures

List of Tables

List of Abbreviations

CDS: Coding Sequence

Cryo-EM: Cryogenic Electron Microscopy

DZD: Delpazolid

LZD: Linezolid

ORF: Open Reading Frame

pLogo: Probability Logo

PTC: Peptidyl Transferase Center

RNC Complex: Ribosome-Nascent Chain Complex

RZD: Radezolid

SRC: Stalled Ribosome Complex

TE: Translation Efficiency

tRNA: Transfer RNA

TZD: Tedizolid

Introduction

The peptidyl transferase center of the ribosome (PTC), situated within the large ribosomal subunit, catalyzes peptide bond formation. Within the PTC, peptide bond formation occurs between the C-terminal amino acid of the nascent chain, tethered to the P-site tRNA (P-tRNA), and the incoming amino acid delivered in the A site by aminoacyl tRNA (aa-tRNA). Stabilization of the PTC–proximal region of the nascent peptide in a specific, β-strand–like conformation orients the donor substrate for efficient catalysis of peptide bond formation.[1]

Ribosome-targeting antibiotics interfere with various stages of translation,[2,3] and have been demonstrated to inhibit translation when the ribosome encounters specific sequences of amino acids in the nascent chain.[4–6] This phenomenon of context-specific inhibition of translation has been documented for numerous exit tunnel-binding antibiotics, including a variety of macrolide antibiotics[7,8] and polyketide tetracenomycin X,[9] for PTC targeting inhibitors, such as chloramphenicol and linezolid,[10–14] as well as for other ribosome-binding antibiotics.[15–17] While detailed analysis of specific antibiotic-dependent stalling sequences has been made possible by structural evaluation of drug-arrested translation complexes,[9,11,12,18–22] we lack a broader understanding of the mechanisms of context-specificity. More recent structural data points to a combination of effects by which stalling may occur in the presence of antibiotics, including allosteric modulation of critical PTC nucleotides and forcing PTC substrates into conformations which preclude successful peptide bond formation. A deeper understanding of the interplay between these mechanisms and how they are affected by structural differences within the antibiotic requires further exploration. Such studies would greatly benefit from antibiotics with related chemical structures but different context-specificity of action.

The oxazolidinone class of antibiotics[23] provides an ideal starting point for exploring the structural dependence of context-specific stalling (Fig. 1A). Linezolid[24,25] (LZD), the first approved oxazolidinone antibiotic, and tedizolid[26] (TZD), a more recently developed derivative, are clinically used for the treatment of Gram-positive bacterial infections. A related oxazolidinone derivative, radezolid[27,28] (RZD), is in clinical development for the treatment of bacterial acne and community-acquired pneumonia. While distinct in their C and D rings, LZD and RZD share the C5-acetamidomethyl functionality. Both LZD and RZD inhibit translation in a context-dependent manner, with Ala in the penultimate position of the nascent peptide [Ala(-1)] as the critical sequence determinant. Cryo-EM analysis of LZD- and RZD-stalled ribosome complexes revealed the critical importance of the C5-acetamidomethyl group of these antibiotics in stabilizing antibiotic binding to the ribosome and the formation of a peptide binding pocket complementary in shape to Ala(-1). Interestingly, although early structure-activity relationship analysis indicated the necessity of the C5-acetamidomethyl group for bacterial growth inhibition,[24] TZD lacks this functional group and, instead, carries a C5-hydroxymethyl substituent. The critical role of the C5 moiety of LZD and RZD in context-dependent stalling prompted us to investigate how replacement of this group with a smaller hydroxymethyl substituent affects translation inhibition.

Here, we use *in vivo* ribosome profiling and *in vitro* toeprinting to show that TZD, as well as an investigational oxazolidinone delpazolid[29] (DZD, Fig. 1A), which also contains the C5-hydroxymethyl group, exhibits context-specificity different from that of LZD and RZD. TZD and DZD preferentially stall the ribosome when isoleucine or histidine appear in the penultimate (-1) position of the nascent chain. Cryo-EM analysis of high resolution TZD- and DZD- stalled ribosome complexes revealed that Ile(-1) and His(-1) nascent peptides stabilize binding of these

antibiotics through structurally distinct mechanisms enabled by a wider peptide binding pocket created by the C5-hydroxymethyl moiety. Strikingly, this wider pocket allows the Ile(-1)–containing nascent peptide to adopt a compact, helical conformation in the presence of TZD and DZD. This novel peptide path stabilizes multiple rRNA nucleotides in orientations that disfavor peptide bond formation. Conversely, structural analysis of stalled complexes with a His(-1)–containing peptide shows an elongated conformation of the nascent chain wherein the oxazolidinone reorients the imidazole side chain of His(-1), resulting in a stabilizing network of interactions that favors stalling.

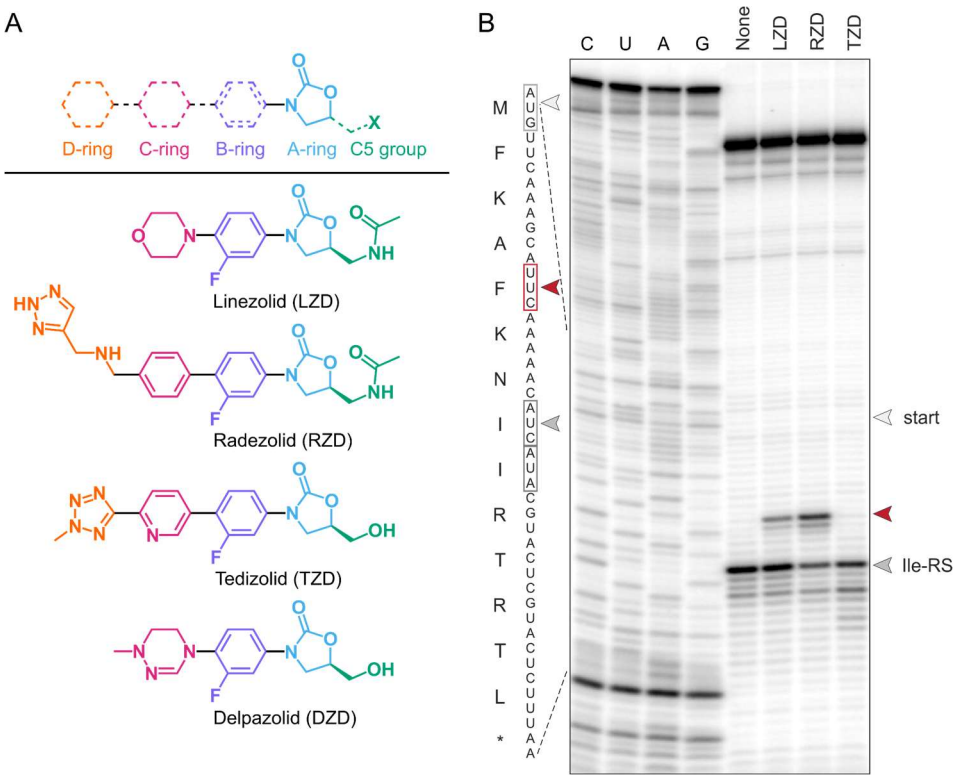

Figure 1: Tedizolid exhibits altered context-specificity compared to linezolid and radezolid. **A)** Structures of oxazolidinone antibiotics. Oxazolidinone antibiotics are composed of a modular multi-ring structure, with variation at the C/D rings and the oxazolidinone C5 substituent. **B)** Ribosome toeprinting performed on a model stalling mRNA in the presence of DMSO, LZD (50μM), RZD (10μM), or TZD (25μM). Stalling with Ala(-1) is indicated in red. Translation beyond the expected stall site is inhibited by isoleucyl-tRNA synthetase inhibitor mupirocin (50μM) present in all reactions (dark gray).

Results

Tedizolid exhibits altered context-specificity compared to linezolid and radezolid

To explore whether the stalling preference of TZD matches that of LZD and RZD, we performed ribosome toeprinting to examine the effect of this antibiotic on synthesis of a peptide containing the MFKAF stalling motif (Fig. 1B). It was previously shown that both LZD and RZD stall translation of this model peptide when Ala reaches the -1 position of the nascent chain.[10,11,13] *In vitro* transcription-translation was performed using *E. coli* ribosomes, in the presence or absence of drug. Ile-tRNA synthetase inhibitor mupirocin was included in all reactions to "catch" any ribosomes that progressed beyond the anticipated stall site.

Treatment with LZD or RZD resulted in a buildup of truncated product corresponding to Ala(-1) stalling, consistent with previous profiling[10] and structural[11] data. Surprisingly, no stalling was observed at this site in the presence of TZD. Instead, translation continued until the ribosome reached the "catch" codon. Thus, TZD appears to act in a context-specific manner distinct from that of LZD and RZD.

Ribosome profiling reveals altered specificity of tedizolid-induced ribosome stalling

We used ribosome profiling as an unbiased strategy to identify stalling preferences of TZD. Oxazolidinone-susceptible *E. coli* strain BW25113 *ΔacrB* was treated with an excess of TZD, and Ribo-seq and RNA-seq libraries were prepared as previously described.[30] Genes with >20% coverage and an average read count of ≥0.5 across the coding sequence (CDS) were considered for downstream analysis.

Ribo-seq reads mapped to the *E. coli* genome showed a clear 3-nt periodicity, attesting to the high quality of the Ribo-seq data,[30] whereas as expected, RNA-seq reads remained codon-independent (Extended Data Fig. 1A). Both Ribo-seq and RNA-seq datasets highly correlated between replicates (Extended Data Fig. 1B). Compared to DMSO control, TZD treatment led to a marked increase in ribosome density within the first ~30% of open reading frames (ORFs) transcriptome-wide, and a concomitant decrease in read density in the latter half of the ORFs (Fig. 2A), consistent with the drug acting as an elongation inhibitor.[31,32] Notably, no individual gene transcripts appeared to be particularly affected, with comparable translation efficiency (TE) scores, defined as a ratio between Ribo-seq and RNA-seq reads, in both treated and untreated samples (Extended Data Fig. 2A). Despite relatively unchanged total TE scores, clear drug-induced stalling peaks are visible, especially toward the 5' regions of example genes *typA* and *ispH* (Fig. 2B,C).

We next analyzed bias in amino acid occurrence at sites of TZD-mediated ribosome stalling. pLogo analysis of the top 1000 sites with increased ribosome occupancy in the presence of TZD revealed a clear dependence on the penultimate (-1) position of the nascent chain for stalling (Fig. 2D). In stark contrast to the well-documented Ala(-1)–dependent LZD-induced ribosome stalling preference,[10,11,13] we observed a significant preference for Ile in the -1 position (23.45% of the top 1000 sequences) in the presence of TZD. Besides Ile(-1), stalling was also observed when the penultimate position of the nascent chain in the drug-arrested ribosome was occupied by Gln (11.02%) and His (6.91%), indicating a dramatically distinct and also broader penultimate amino acid preference for TZD compared to LZD. As with linezolid, Gly is disfavored in the penultimate and C-terminal position of the nascent chain and as the A-site incoming amino acid.

To evaluate transcriptome-wide stalling preference of TZD, we averaged the change in frequency of occurrence of each amino acid within the ten C-terminal residues of the nascent chain and the incoming amino acid, across all stalling codons transcriptome-wide (Fig. 2E). In agreement with the trends observed in the pLogo charts, the most pronounced changes in occurrence were observed for nascent chains with penultimate Ile, His, or Gln. To a lesser degree, stalling was also observed with Cys(-1), further emphasizing the broad -1 dependence of TZD-induced stalling. As with the top stall sites (Fig. 2D), we observed a strong preference against Gly(-1).

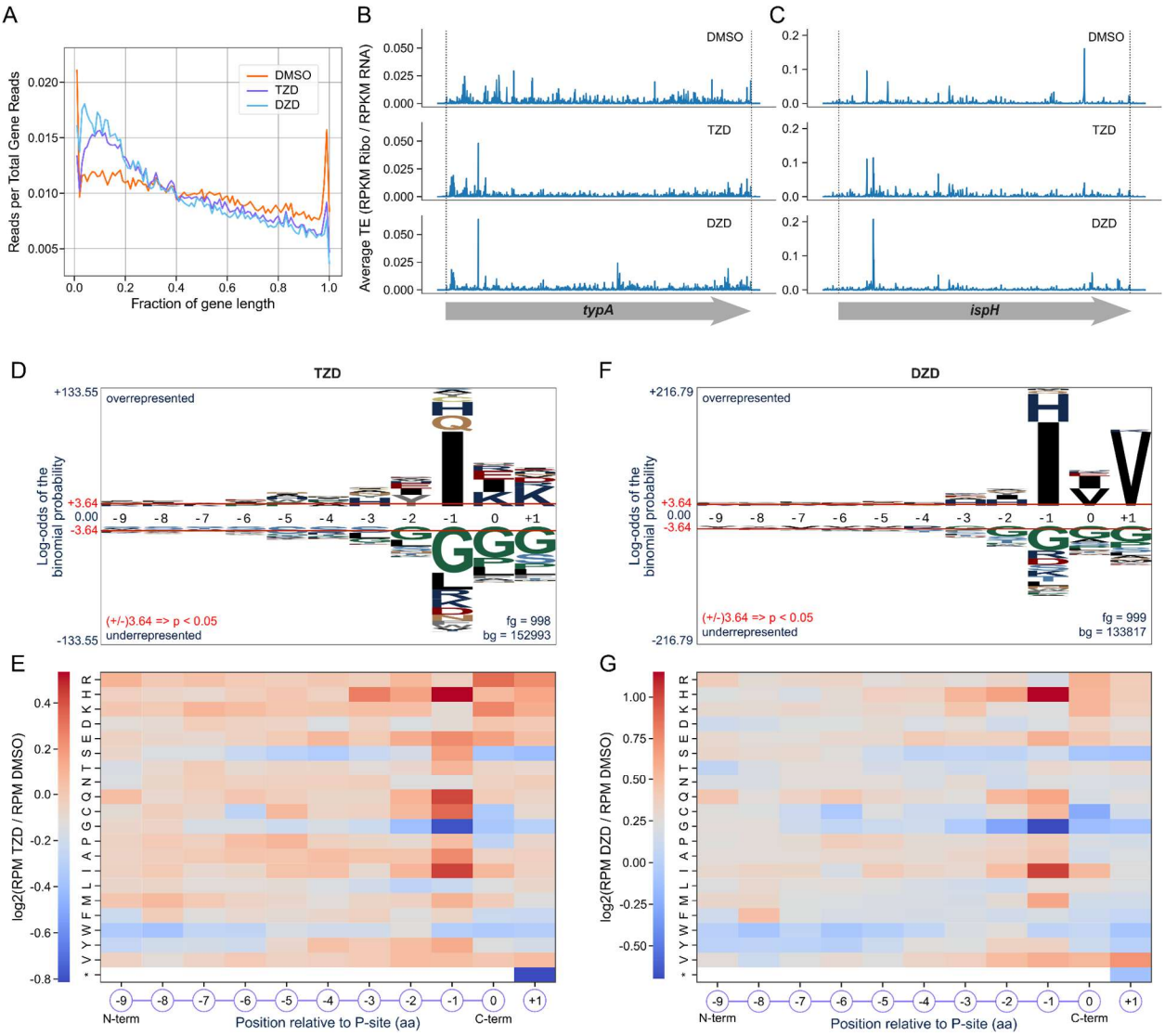

Figure 2: Ribosome profiling reveals unique stalling preferences of tedizolid and delpazolid.

A) Metagene analysis of ribosome profiling data following 2.5 min treatment with 10x MIC TZD (20 µg/mL) or DZD (80 µg/mL). Positions within coding regions were normalized to gene length, and reads at each position were averaged across all ORFs. **B and C)** Redistribution of ribosome stalls across the B) *typA* or C) *ispH* open reading frames. Both genes show a clear drug-induced peak near the 5' end and comparable overall translation efficiency. **D-G)** Codon-level analysis of stalling preferences within the top 1000 stall sites (D: TZD treated, F: DZD treated) or across the entire transcriptome (E: TZD treated, G: DZD treated). Individual stall sites were ranked as a function of log2 fold change in pause score between conditions, where pause score is defined as RPKM[codon]/ RPKM[gene]. **D, F)** pLOGO[52] analysis utilized the top 1000 stall sites as foreground and the remaining sites as background. **E, G)** Transcriptome-wide heatmaps were produced by averaging reads per million for every instance of an amino acid occurring at positions -9 to +1 of a nascent chain and taking the log2 fold change relative to DMSO control.

Delpazolid exhibits enhanced stalling with nascent peptides containing penultimate Ile or His

Despite overall chemical similarity, our findings revealed distinct stalling preferences for TZD compared with LZD. A key distinguishing feature of the two antibiotics is the C5 moiety of the oxazolidinone ring, where the acetamidomethyl group of LZD is replaced by an alcohol moiety in TZD (Fig. 1A). We hypothesized that the nature of the C5 substituent may contribute to altered stalling preference. To test this hypothesis, we turned to ribosome profiling with DZD (Extended Data Fig. 3, Fig. 2), an oxazolidinone compound active against methicillin-resistant *S. aureus*, as well as multidrug-resistant and extensively drug-resistant tuberculosis.[29,33] While the ring system of DZD is more comparable to that of LZD, DZD shares the truncated C5-hydroxymethyl moiety with TZD (Fig. 1A). DZD thus provides a valuable model system for exploring the role of the C5 substituent in determining context-specificity of oxazolidinones.

Much like TZD, DZD caused a buildup of ribosome occupancy early in ORFs (Fig. 2A). At the codon level, however, DZD-induced ribosome stalling sites showed a narrower preference in the nascent chain penultimate position compared to TZD. Analysis of both the top stall sites and transcriptome-wide stalling motifs resulting from DZD treatment showed a strong preference for Ile(-1) and His(-1) (33.03 % and 13.01% in the top 1000 sites, respectively; Fig. 2F,G). We also observed a preference for Val as the incoming amino acid and an exclusion of Gly, particularly at the -1 position.

Taken together, our findings from Ribo-seq experiments suggest that TZD and DZD preferentially stall translation after Ile or His have been incorporated into the penultimate position of the nascent peptide. This is in stark contrast to LZD and RZD, which strongly prefer

Ala at this position, supporting the hypothesis that the chemical nature of the oxazolidinone C5 substituent dictates ribosome arrest preference.

Context-dependency of TZD- and DZD-induced translation arrest can be recapitulated in vitro

To validate the identified stalling motifs within specific sequence contexts, we used the ribosome profiling data to select five genes with representative ribosome stall sites where the nascent chain would contain either Ile or His in the penultimate position (Fig. 3A,C, Extended Data Fig. 4). While the effects of the two antibiotics are largely similar, DZD-induced peaks of increased ribosome occupancy appear to be generally more prominent and specific than TZD-induced stalls. These observations are consistent with a more narrow specificity of DZD-induced stalling (Fig. 2F,G), as compared to TZD (Fig. 2D,E).

The selected stall sites were evaluated *in vitro* by toeprinting analysis, as described above. For these, we designed templates that encoded 5-7 amino acids preceding the anticipated site of drug-induced arrest, using either the gene's natural start codon or introducing a new start codon at the appropriate distance from the stall site.

The isoleucine-containing NTA**I**KW peptide derived from the *typA* gene showed a particularly strong drug-induced ribosome stalling signal in the Ribo-seq data and was therefore used in the initial toeprint experiments (Fig. 3A,B). In the presence of LZD, ribosome stalling occurred only when Ala4 of the template was in the penultimate position of the nascent peptide, consistent with the previously established stalling preference.[10,11] While we also observed a faint band at this position for TZD and DZD, both drugs also induced stalling at the next codon, when Ile appeared in position -1 of the nascent chain. Consistent with the ribosome profiling data, the Ile(-1) stalling bands were stronger under DZD treatment than under TZD treatment. An

additional faint band placing Trp in the -1 position was observed (Fig. 3B). In agreement with the Ribo-seq data, ribosome arrest at the stall sites was incomplete, and a large fraction of ribosomes were able to reach the Arg11 "catch" codon, where they were arrested due to the presence of an Arg tRNA-synthetase inhibitor in the reactions.

To further evaluate oxazolidinone-induced Ile(-1)–dependent stalling, we carried out toeprinting analysis using the *dcuA* transcript, which contains the TZD- and DZD-induced stalling site within the VVELIIV motif (Extended Data Fig. 4A-C). In the cell-free translation system, two distinct stall sites were observed within this sequence in the presence of either TZD or DZD: one with penultimate Leu, and another with the first of two consecutive Ile residues in the -1 position. The exact placement of the drug-stalled ribosome within this template was further verified by using Ile tRNA-synthetase (Ile-RS) inhibitor mupirocin, whose presence causes ribosome stalling during decoding of A-site (+1) Ile. The penultimate Ile stall site induced by TZD and DZD is positioned one codon after the mupirocin-induced site, in line with their differing modes of action. These results confirm the importance of the penultimate Ile for stalling, while also suggesting a more relaxed sequence dependence of TZD and DZD action in the cell-free translation system in comparison with cellular translation.

We used Ribo-seq data to select two genes, *ettA* and *ispH*, to evaluate the importance of penultimate His for TZD- and DZD-induced stalling *in vitro* (Fig. 3C,D, Extended Data Fig. 4D-F). In contrast to LZD, DZD and TZD treatment resulted in distinct toeprint bands within the *ettA* and *ispH* templates. These stalls placed the arrested ribosome one codon down from the respective His codons, thereby confirming that the penultimate His residue in the nascent peptide is conducive to the drug-induced translation arrest. These findings were further corroborated with the *rhlB* template (Extended Data Fig. 4G-I). As with the Ile(-1) stall sites, the arrest was more

prominent with DZD than with TZD. Inspection of the stronger stall sites in each sequence revealed the presence of Arg preceding the penultimate His residue, matching an [R/K]HXX motif suggested by pairwise analysis of stall sites from the ribosome profiling for both TZD and DZD (Extended Data Fig. 5).

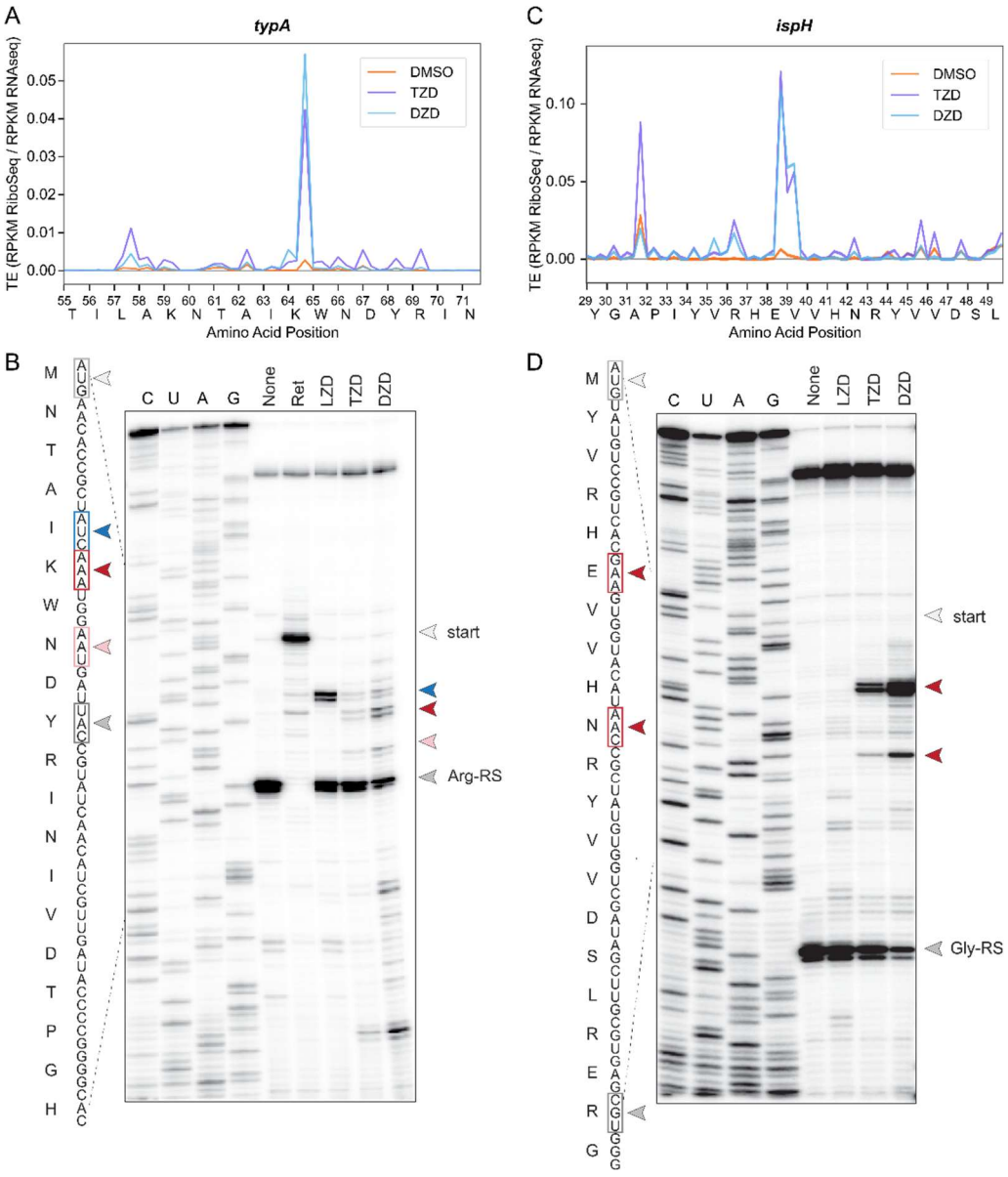

Figure 3: Validation of tedizolid and delpazolid-induced stall sites.
A) Ribo-Seq traces of TZD (purple) and DZD (blue) indicate Ile(-1)-dependent stalling during translation of NTAIK sequence within the *typA* ORF compared to DMSO (orange). **B)** Ribosome toeprinting on a *typA*-derived NTAIKW mRNA template in the presence or absence of LZD, TZD, or DZD. Stalling with Ala(-1) is denoted in blue, Ile(-1) in red, and Trp(-1) in pink. Retapamulin was used to induce stalling at the start codon (light gray). Arginine tRNA-synthetase inhibitor (Arg-RS, dark gray) was included in all reactions to "catch" any ribosomes that progressed beyond oxazolidinone-dependent stall sites. **C)** Ribo-Seq traces within the *ispH* ORF indicate TZD- and DZD-dependent stalling with His(-1) at YVRHE. **D)** Toeprinting on an *ispH*-derived YVRHEV mRNA template in the presence or absence of LZD, TZD, or DZD. Stalling with His(-1) is denoted in red. Glycine tRNA-synthetase inhibitor (Gly-RS, dark gray) was included in all reactions to "catch" any ribosomes that progressed beyond the oxazolidinone-dependent stall sites. All compounds were treated at 50 µM for toeprinting reactions.

Stalling at penultimate isoleucine induces a novel stalled peptide conformation

Having shown that TZD and DZD exhibit Ile(-1) stalling, we aimed to identify the molecular basis of this specificity. Stalled ribosome complexes (SRCs) were produced via *in vitro* transcription-translation of an MNTA**I**K template using *E. coli* ribosomes in the presence or absence of TZD. To favor the formation of a homogeneous complex and allow for the preparation of a drug-free ribosome-nascent chain (RNC) complex, the coding sequence was truncated after the Lys6 codon to generate a stop-less mRNA. The complex generated from the cell-free system was purified and applied to cryo-EM grids. Homogeneous refinement yielded a 2.16Å resolution map of the TZD-MNTAIK SRC, with well-defined density for TZD (Fig. 4A,B, Supplementary Table 1, Supplementary Fig. 1, Extended Data Fig. 6A). Modeling and real-space refinement unambiguously placed Ile in the penultimate position of the nascent MNTAIK peptide (Fig. 4B). This peptide assignment was further verified via analysis of density in the decoding center, which matched the AAA-Lys codon and tRNA-Lys in the P-site (Extended Data Fig. 6B).

We next compared this TZD-stalled complex with previously published LZD-MFKAF and RZD-MFKAF SRCs. The A, B, and C rings of these drugs showed a near-identical placement (Fig. 4C). TZD binding is stabilized by a number of interactions with the ribosomal RNA in the stalled complex (Fig. 4D). In particular, π-π stacking between the oxazolidinone B-ring and C2452, as well as coordination of a nearby Mg^{2+} ion via the A-ring carbonyl moiety, are consistent with previously observed interactions in LZD and RZD.[11] The D-ring of TZD forms a hydrogen-bond interaction with A2602. This residue engages RZD via π-π stacking and is unavailable for interaction with the shorter LZD ring system. We observed a major difference in the positioning of the C5 substituents emerging off the A ring. While the longer acetamidomethyl

substituents of LZD and RZD fold toward the nascent peptide chain, the hydroxyl group of the C5-hydroxymethyl substituent of TZD extends towards the exit tunnel wall (Fig. 4C), resulting in a wider peptide pocket (Fig. 4E) for TZD compared to LZD- and RZD-containing ribosome complexes. This rotation is supported by a hydrogen bond with the backbone of G2505 in 23S rRNA (Fig. 4D).

In contrast to the nearly identical positioning of the different oxazolidinones, the nascent chain in the TZD-SRC assumes a conformation that drastically differs from the largely extended conformation of the MFK**A**F nascent peptides in the LZD- and RZD-stalled complexes[11] (Fig. 4C). The MNTA**I**K nascent peptide assumes an i+3 helical conformation, enforced by hydrogen bonding between the backbone amides of Lys(0) and Thr(-3) as well as Ala(-2) and Met(-5) (Fig. 4B,F). In this helical conformation, Ile(-1) can form two potential CH-π bonds with the B-ring of TZD via its α or γ carbon (Fig. 4D). Distances and $C\text{-}H_{(pred)}$-π angles for both of these putative interactions are consistent with established constraints for CH-π bonding.[34] The novel peptide path is further stabilized by hydrogen bonding between the Ile(-1) backbone carbonyl and G2061, as well as an Ala(-2)–U2506 CH-π interaction (Fig. 4F). We additionally solved the cryo-EM structure of a DZD-SRC with the same peptide. The resulting 2.80Å DZD-MNTAIK SRC (Supplementary Table 1, Supplementary Fig. 1, Extended Data Fig. 6A) structure revealed that the peptide backbone adopts a similar compacted helical conformation, positioning the C5-hydroxymethyl group towards the tunnel wall and the penultimate Ile towards the antibiotic (Fig. 4G).

To test whether the unusual conformation is an intrinsic property of the MNTAIK sequence or whether it is specifically induced by the bound antibiotic, we trapped a drug-free complex with MNTAIK-peptidyl tRNA in the PTC using the analogous transcription-translation

strategy in the absence of antibiotic (Supplementary Table 1, Supplementary Fig. 1, Extended Data Fig. 6A). In contrast to the helical conformation of the nascent peptide in the presence of TZD and DZD, we instead observe an extended nascent chain trajectory in the absence of antibiotics (10.0Å measured from Cα of Lys(0) to the Cα of Asn(-4), versus 6.8Å in the TZD-stalled complex and 6.9Å in DZD-stalled complex; Extended Data Fig. 7A). Interestingly, this elongated conformation would place Ile(-1) in direct steric clash with the bound oxazolidinone (Fig. 4H, Extended Data Fig. 7B). The comparison of the drug-free and drug-bound structures therefore illuminates an important concept – that PTC-bound antibiotic is able to alter the trajectory of the nascent protein chain in the exit tunnel.

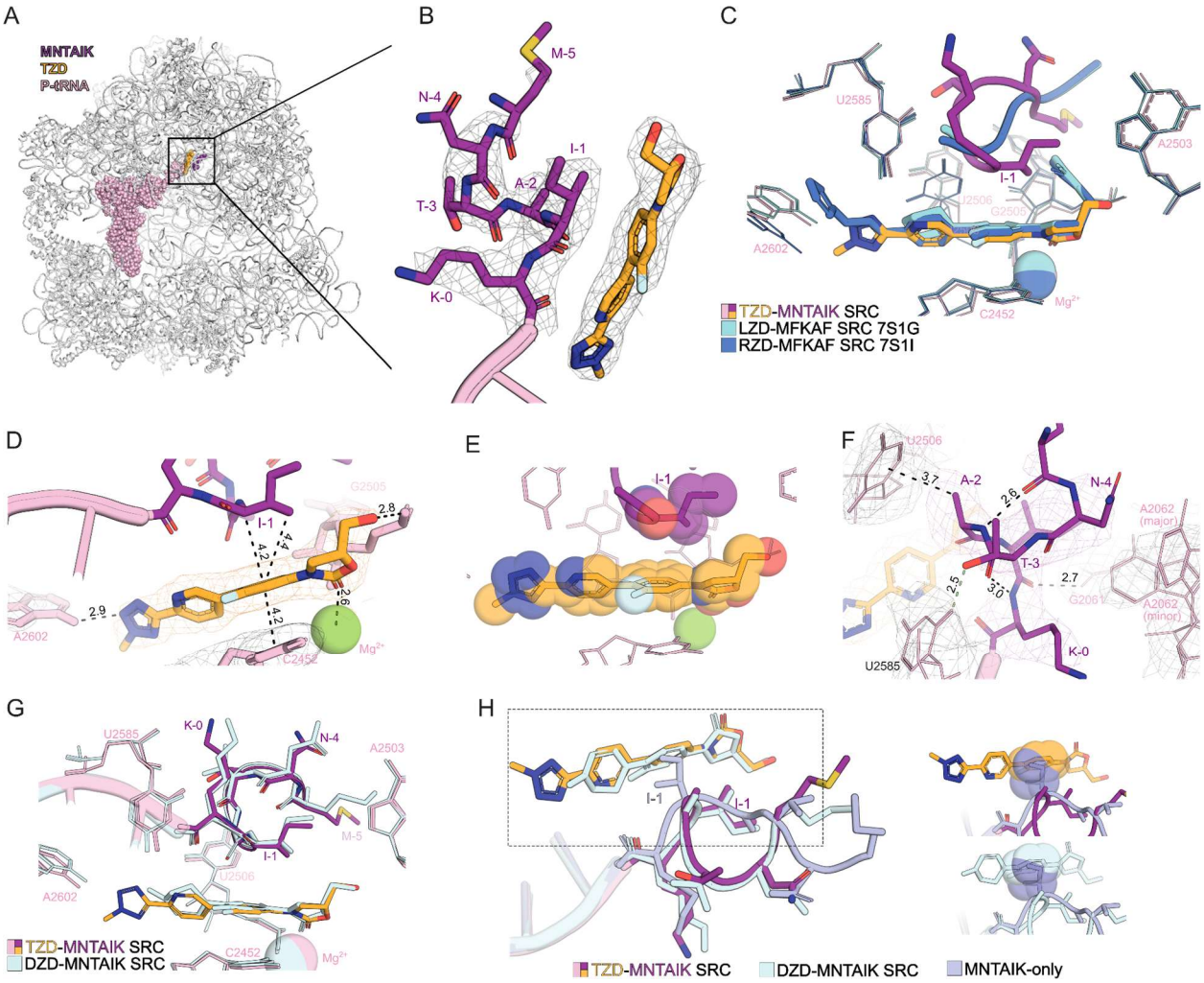

Figure 4: Tedizolid-induced ribosome stalling alters conformation of nascent peptide. **A)** Cross-section of the cryo-EM density map of the TZD-stalled 70S *E. coli* ribosome in complex with peptidyl-tRNA (TZD-MNTAIK SRC). **B)** Close-up of TZD (gold) in complex with MNTAIK arrest peptide (magenta). **C)** Alignment of TZD binding site and nascent chains with those of previous oxazolidinone stalled complexes: LZD-MFKAF SRC (PDB 7S1G, teal) and RZD-MFKAF SRC (PDB 7S1I, blue). **D)** Direct interactions between TZD and 23S rRNA (pink) or peptide (magenta). Dashed black lines represent binding interactions; distances are shown in Å. **E)** Spheres representation of TZD interaction with penultimate Ile. Spheres contour highlights the shape complementarity between the drug and the peptide. **F)** Direct interactions between MNTAIK arrest peptide and 23S rRNA residues, represented by dashed black lines with distance in Å. A lower confidence interaction with the side chain of T(-3) is shown in green. **G)** Comparison between the TZD-MNTAIK SRC (pink) and DZD-MNTAIK SRC (cyan). **H)** Overlay of peptide path for the TZD-MNTAIK SRC and an analogous drug-free MNTAIK RNC (lavender). Right: spheres representation of the clash between TZD/DZD and Ile(-1) of the drug-free peptide complex.

His(-1) stalling by TZD and DZD is distinct from that at Ile(-1)

In order to explore the mechanism of stalling at penultimate histidine, we prepared SRCs from an ispH-derived stopless MYVRHE template, in the manner described above, yielding a 2.78Å TZD-stalled ribosome complex with clear density for the bound oxazolidinone and His in the penultimate position (Fig. 5A). This assignment was verified via P-tRNA and decoding center densities matching tRNA-Glu and codon GAA, respectively (Extended Data Fig. 6C).

The TZD binding pose in the His(-1) SRCs bears a strong similarity to that observed in our structures with penultimate Ile (Fig. 5B). As with the TZD-MNTAIK SRC, the C5-hydroxymethyl moiety of tedizolid in the TZD-MYVRHE SRC faces away from the peptide and engages in a hydrogen bond with G2505 in the 23S rRNA, while the B-ring of the antibiotic stacks with C2452 and the oxazolidinone carbonyl coordinates with Mg^{2+} (Fig. 5C). A carbonyl-π interaction between U2585 and the electron-rich aromatic C-ring of TZD, permitted by a shift in position of the rRNA nucleotide, may stabilize the drug binding on this complex (Fig. 5C), supplementing a lost A2602 interaction due to repositioning of the nucleotide. Despite the near identical binding pose of the drug, the MYVRHE peptide orientation is highly divergent from that of MNTAIK stalled by the same oxazolidinone. Rather than forming a helix, as in the MNTAIK SRCs, the MYVRHE peptide takes on the more expected β-strand–like conformation (Fig. 5A,B). As in previous oxazolidinone stalled complexes, we observe a CH-π interaction between the oxazolidinone B-ring and the β-carbon of the penultimate amino acid (Fig. 5C,D). Unusually, however, a second CH-π interaction is apparent between the elbow of the C5-hydroxymethyl group and the His(-1) imidazole. Hydrogen bonds with the exocyclic amine of A2062 and the ring oxygen of the ribose of G2505 additionally sandwich His(-1) into position. The nascent chain is further stabilized by hydrogen bonds between the peptide backbone and

rRNA nucleotides U2506, A2061, and A2062, and a salt bridge between R(-3) and E(0) favors the extended peptide conformation (Fig. 5D).

We additionally prepared a delpazolid-stalled MYVRHE complex for comparison (Supplementary Table 1, Supplementary Fig. 1, Extended Data Fig. 6A). Positioning of DZD was once again unchanged from that in the Ile(-1) complex (Fig. 5E). The peptide path in the DZD-stalled complex perfectly matched that observed in the TZD-MYVRHE SRC, with a conserved set of interactions stabilizing drug binding (Extended Data Fig. 8A). We also compared the conformation of the nascent peptide in a drug-free stalled complex to that of the drug-bound MYVRHE SRC (Fig. 5F). In contrast to major changes in backbone conformation observed in Ile(-1) containing stalled complexes, the backbone conformation of His(-1) stalled peptide is largely unchanged by the presence of the drug. A flipped His(-1) side chain in the drug-free RNC, the only notable difference, would prevent binding of either oxazolidinone (Fig. 5F). Although the side chain interactions of histidine are lost in this flipped conformation, the remainder of the peptide is still stabilized by the same backbone H-bonds as in the two His(-1) stalled complexes (Extended Data Fig. 8B). Together, these data suggest that drug-induced reorientation of the histidine side chain, and the stabilization of the repositioned His through a number of favorable interactions with both antibiotic and rRNA, accounts for His(-1)-dependent stalling of the ribosome.

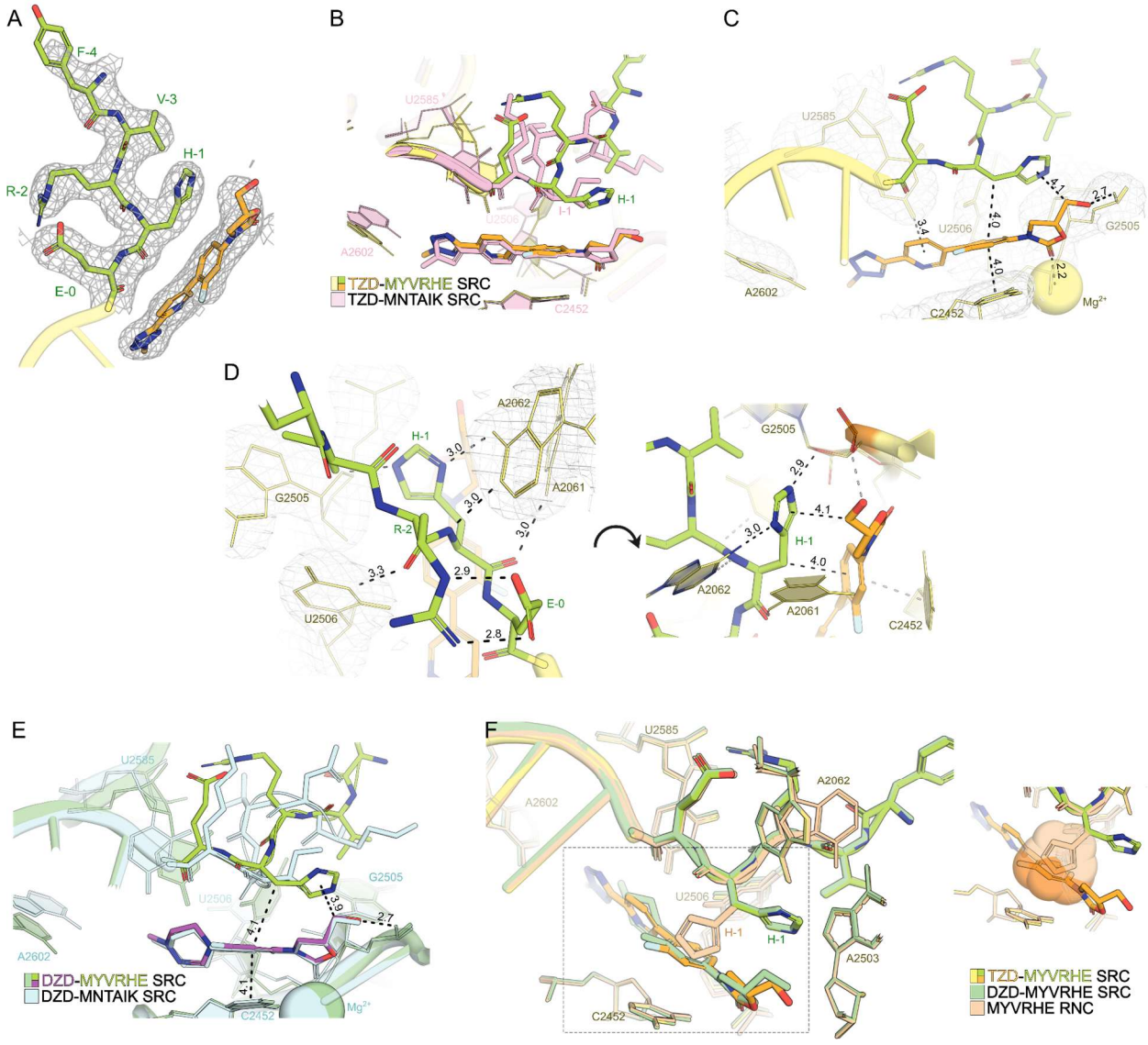

Figure 5: Oxazolidinone stalling at His(-1) mechanism differs from Ile(-1) stalling.
A) Close-up of TZD (gold) in complex with MYVRHE arrest peptide (lime). **B)** Comparison of peptide path and drug positioning in the TZD-MYVRHE SRC (rRNA, tRNA: yellow, TZD: gold, MYVRHE peptide: lime) and TZD-MNTAIK SRC (pink). **C)** Direct interactions between TZD and 23S rRNA or peptide on the MYVRHE SRC. Interactions are indicated by dashed black lines with distances in Å. **D)** Direct interactions between TZD-stalled MYVRHE nascent chain and 23S nucleotides. Histidine interactions are highlighted in the right panel with distances in Å. **E)** Comparison of peptide path and drug positioning in the DZD-MYVRHE (rRNA, tRNA: green, DZD: purple, MYVRHE peptide: lime) and DZD-MNTAIK (cyan) SRCs. Interactions on the DZD-MYVRHE SRC are shown in black dashed lines with distances in Å. **F)** Overlay of the TZD-MYVRHE (yellow, gold, lime) and DZD-MYVRHE (green) stalled complexes with a drug-free RNC from the same peptide (wheat). Inset: spheres representation of clash between His(-1) of MYVRHE RNC (wheat) and TZD (gold).

Drug-induced nascent peptide stalling affects conformation of surrounding rRNA nucleotides

Translation arrest resulting from cooperation between the antibiotic and the nascent peptide has been shown to affect conformations of the surrounding rRNA,[11,18–20,22] motivating our investigation into the orientation of adjacent nucleotides in our SRCs (Fig. 6). Our comparative structural analysis indicates that both the presence of the drug and the sequence of the nascent peptide profoundly influence nucleotide conformation in rRNA.

In Ile(-1) containing SRCs, nucleotide A2062 appears to be far more flexible in the drug-stalled complexes compared to the peptide-only RNC (Fig. 6A). We observe two populations in the TZD- and DZD-SRCs for A2062; the minor orientation of A2062 (~40% in the TZD-SRC) is involved in a non-canonical Hoogsteen base pair with nearby nucleotide A2503, while the majority population is rotated towards the tunnel lumen. By contrast, the MNTAIK-only RNC favors the lumen conformation exclusively. Interestingly, this pattern differs from what was previously observed with LZD, where paired orientation of A2062 was stabilized in the LZD-MFKAF SRC relative to the dual conformation observed in a LZD-only ribosome complex.[11] Nucleotide U2585 also shifts in the drug-stalled complexes in comparison with the drug-free RNC to accommodate the novel peptide path, assuming a position similar to that observed in the LZD-SRC. In Ile(-1) stalled complexes, nucleotide U2506 also undergoes significant rotation towards the tunnel wall, into a conformation that has been associated with a catalytically nonproductive state of the ribosome.[20,35,36] This rotated orientation of U2506 avoids steric clash with Ala(-2) in the compacted peptide, and instead enables a CH-π interaction between the two. This rotated state is akin to one observed in the LZD-MFKAF SRC, despite its extended peptide, but differs from the one observed in the RZD-MFKAF SRC from the same source. In the presence of both antibiotics, we also observe repositioning of the highly flexible nucleotide

A2602 in the stalled complexes relative to the RNC, nearer to the orientation observed in the LZD SRC. As drug-induced stabilization of this nucleotide has been suggested to contribute to ribosome stalling by steric interference with incoming aminoacyl-tRNA,[9,19,20,37] this slight shift towards the A-site may contribute to the stalling mechanism.

In contrast to the Ile(-1) containing SRC structures, we observe only minimal adjustment of rRNA nucleotides between the drug-stalled and peptide-only His(-1) complexes. In the presence of TZD or DZD, A2062 is stabilized in the base-paired conformation, but takes on two orientations in the MYVRHE-alone complex. A ~0.7Å shift in the position of U2585 between the TZD/DZD-MYVRHE SRCs and the LZD SRC enables a potential interaction between the nucleotide carbonyl and the C-ring of the oxazolidinone (Fig. 6B, 5C). The shift in U2585 and lack of rotation in U2506 in the His(-1) SRCs and RNC brings their positions nearer to those of the MNTAIK-alone complex. A2602 is also shifted beyond its position in the LZD-SRC such that interaction with the TZD D-ring becomes unlikely in the His(-1) complex.

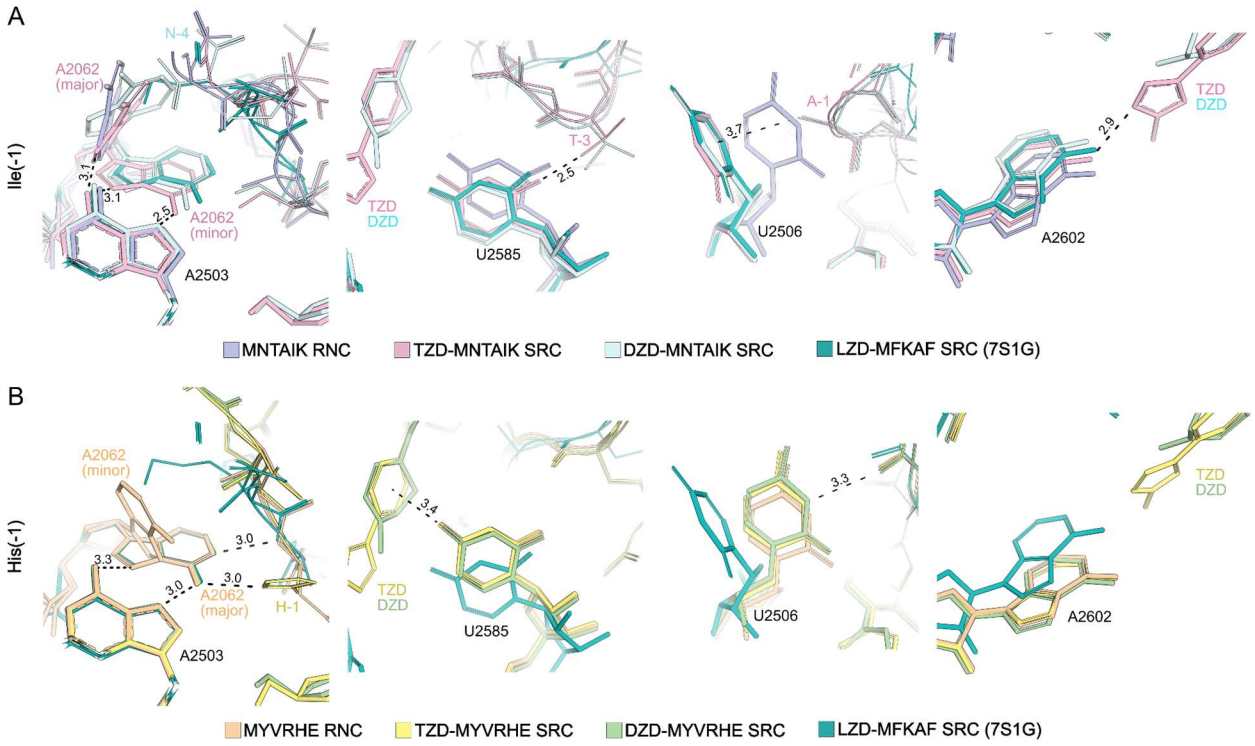

Figure 6: Oxazolidinone-mediated stalling at nascent peptides affects rRNA positioning. Comparison of 23S rRNA nucleotide positions in **A)** Ile(-1)-containing complexes (MNTAIK RNC: lavender, TZD-MNTAIK SRC: pink, DZD-MNTAIK SRC: cyan) or **B)** His(-1)-containing complexes (MYVRHE RNC: orange, TZD-MYVRHE SRC: yellow, DZD-MYVRHE SRC: green). Positions of all nucleotides are compared to that of LZD-MFKAF SRC (teal; PDB 7S1G). Dashed lines show interactions of the TZD complex for each set with distances in Å.

Discussion

Our investigation into the mechanism of translation inhibition by oxazolidinone antibiotics TZD and DZD shows that these antibiotics inhibit translation in a context-dependent manner, a feature previously observed for LZD and RZD. In contrast to a requirement for the presence of Ala in the penultimate position of the nascent chain for LZD and RZD-induced ribosome stalling, both TZD and DZD preferentially stall translation of nascent peptides containing Ile or His as penultimate residues. The stalling preference is extended for TZD to encompass Gln(-1) as well. The novel sequence preference of these oxazolidinones likely stems from the presence of a shorter C5-hydroxymethyl side chain in TZD and DZD, which allows for a wider peptide path and accommodation of larger side-chains at the penultimate amino acid residue of the nascent chain.

Structural analysis of TZD- and DZD-bound ribosomes stalled with the Ile(-1) containing nascent peptide revealed a novel, compact trajectory of the growing protein chain, distinct from the extended conformations observed in other drug-stalled complexes analyzed to date.[9,11,12,18–20,22] This novel conformation represents the first instance of a drug-induced helical conformation of the nascent polypeptide immediately proximal to the P-tRNA (Extended Data Fig. 9). A similarly compact conformation containing a C-terminal helix in the nascent chain was previously observed in the force sensor protein VemP.[38] While the α-helical terminus of VemP is produced from a 20-amino acid stalling motif, oxazolidinone-induced stalling at the MNTAIK peptide achieves helical conformation of a far shorter peptide segment. This novel drug-induced conformation is particularly interesting in light of recent findings that ribosomes stabilize non-arrested peptides in an extended β-strand conformation for more efficient peptide bond

formation,[1] suggesting that altered conformation is likely to play an important role in the mechanism of drug-mediated inhibition of translation. The extended β-strand-like peptide trajectory observed for MNTAIK on the ribosome in the absence of drug further supports this hypothesis.

The observed trajectory of drug-stalled Ile(-1) peptide appears to result from a combination of factors. The drug induces the helical peptide conformation by obstructing its β-strand–like trajectory. The side chain of penultimate Ile is snugly accommodated in this novel conformation by an expanded nascent peptide-facing pocket of the drug. We previously showed that the acetamidomethyl group of LZD sterically occludes a portion of the PTC, creating a smaller pocket that can accommodate only the side chain of Ala.[11] In contrast, the C5-hydroxymethyl substituent of TZD and DZD is pulled towards the exit tunnel wall, thereby widening the amino acid side chain binding pocket. Locked into this conformation by an H-bond with the rRNA backbone, ribosome-bound C5-hydroxymethyl–containing oxazolidinones are less restrictive of larger penultimate residues in the nascent peptide. These larger amino acids are capable of enhanced CH-π interaction with the oxazolidinone, firmly stabilizing its binding on the ribosome. Steric clash between the incoming A-site aminoacyl-tRNA and B-C-D rings of the newly peptide-stabilized oxazolidinone, previously suggested from crystal structures of LZD-bound non-translating ribosomes,[5] is therefore likely the primary contributor to stalling. By precluding formation of a H-bond network previously identified as critical to proper positioning of the peptide for catalysis of peptide bond formation,[1] as in the case of other stalled complexes with modified C-terminal secondary structure[38-41], the helical peptide conformation required for Ile(-1) accommodation may further deter continued translation. In addition, stabilization of critical rRNA nucleotides A2062, U2585, U2506, and A2602 in positions observed in

catalytically incompetent ribosome complexes[22,35,38,42,43] likely impedes flexibility required for ribosome function.

Our TZD- and DZD-stalled complexes with His(-1)-containing peptide have revealed a substantially different nascent peptide conformation compared to that with penultimate isoleucine. As with the Ile complexes, the short C5-OH facing towards the tunnel wall provided a binding pocket better suited to the larger penultimate residue. Rather than altering conformation of the backbone, the His(-1) peptides took on an extended conformation more similar to that observed in the drug-free nascent chain complex and the previous LZD- and RZD-SRCs.[11] The TZD-stalled nascent chain differed from the analogous peptide-only complex only in rotation of the His(-1), preventing steric clash with the drug. In this conformation, His forms two CH-π interactions with TZD, and is further held in position by interactions of the imidazole ring with surrounding rRNA residues. Notably, histidine is one of the few amino acids able to fit in this pocket with an extended peptide conformation; the β-branch of Ile would cause it to crowd the oxazolidinone binding site, while larger aromatic residues capable of the CH-π stabilization would clash with G2505. Interactions between the peptide backbone and rRNA residues A2061, A2062, and U2506 are highly reminiscent of those highlighted in a non-arrested ribosome complex, which orient the nascent chain for peptide-bond formation in a catalytically competent ribosome.[1] Thus, in contrast to the vast disruptions of the oxazolidinone—Ile(-1) complex, stalling at His(-1) appears to rely on locking of the penultimate residue.

While both TZD and DZD show a preference for Ile(-1) or His(-1) at their stall sites, we noted critical differences between the stalling preferences of the two drugs. Compared to DZD, TZD-mediated stalling is inclusive of a wider variety of alternative penultimate nascent chain residues, including Gln(-1) and to a lesser extent Cys(-1). In addition to the narrower -1 stalling

preference, DZD-induced stalling peaks tend to be higher and less frequent than those caused by TZD. This trend was recapitulated by the *in vitro* toeprinting experiments. As a result, treatment with DZD leads to a greater fraction of ribosomes stalling at fewer sites, rather than being distributed across many. The lack of significant differences between our TZD- and DZD-SRCs suggests that while the D-ring is not critical for Ile(-1) and His(-1) stalling, the additional stabilization it provides may enhance stalling even at less favorable sites.

Not every occurrence of Ile, His, or Gln in the nascent peptide leads to pronounced TZD- or DZD-induced translation arrest (Extended Data Fig. 10), suggesting that an expanded sequence context may significantly contribute to stalling, as previously observed for other antibiotics.[15,20] Although TZD and DZD appear to induce stalling at the majority of Ile(-1) and His(-1) sites tested by toeprinting, we noted variation in band intensities for sites containing multiple potential stalling motifs (Fig. 3B,D, Extended Data Fig. 4C,F). Pairwise analysis of the ribosome profiling datasets provided new insights, revealing an [R/K]HXX motif at the stronger His(-1)–containing stall sites of *ispH* and *ettA* (Fig. 3D, Extended Data Fig. 4F, 5A-B). This motif, shared between the two C5-hydroxymethyl oxazolidinones, represents the first instance of expanded specificity beyond the -1 position for this class of compounds. Although our MYVRHE complex contains this motif, we observe no interactions for R(-2) except a salt bridge with E(0). As a charged residue at the P-site does not appear critical for the identified [R/K]HXX motif, charge repulsion between R(-2) and H(-1) may instead favor the β-strand–like extended conformation over a helical path. Alternatively, in the absence of E(0), R(-2) may interact with the rRNA backbone to further stabilize stalling of the nascent peptide, and thus support the network of direct interactions we observe for penultimate histidine.

We have shown that changes in the structure of oxazolidinone antibiotics can lead to major alterations in stalling sequence preferences. Given the importance of context-specific ribosome stalling in mediating the expression of antibiotic resistance factors,[18–20,22,44,45] a better understanding of the molecular contributors to this mechanism is critical to developing antimicrobial compounds capable of averting the induction of resistance genes. In particular, the shared Ala(-1) specificity of LZD and the natural product chloramphenicol (CHL)[10] makes LZD likely to activate expression of CHL-inducible resistance genes.[45,46] With altered stalling specificity, TZD and DZD may prevent this induction. Because activation of many resistance genes relies on the amino acid specificity of the inducing antibiotic, modifications to such specificity could be implemented to improve therapies for multidrug-resistant bacterial infections.

Extended Data

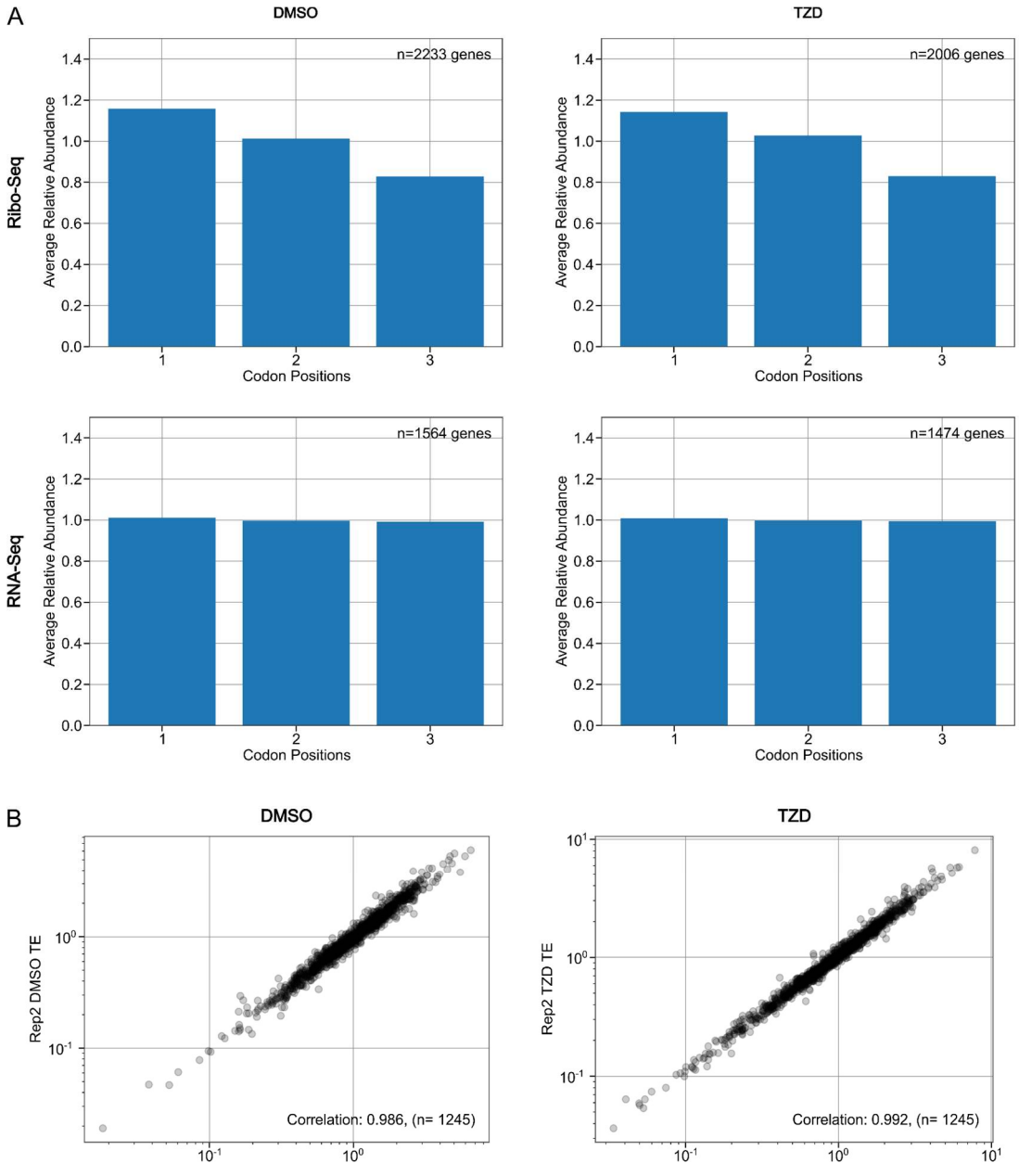

Extended Data Figure 1: Ribosome Profiling Processing After TZD Treatment.
A) Periodicity analysis of profiling data following 2.5 min treatment with DMSO or 10x MIC TZD. Top: Ribosome profiling. Bottom: RNA-seq. **B)** Genewise correlation between replicates. Changes in translation efficiency (RPKM Ribosome profiling/RPKM RNA-seq) for individual genes between experimental replicates following DMSO (left) or TZD (right) treatment.

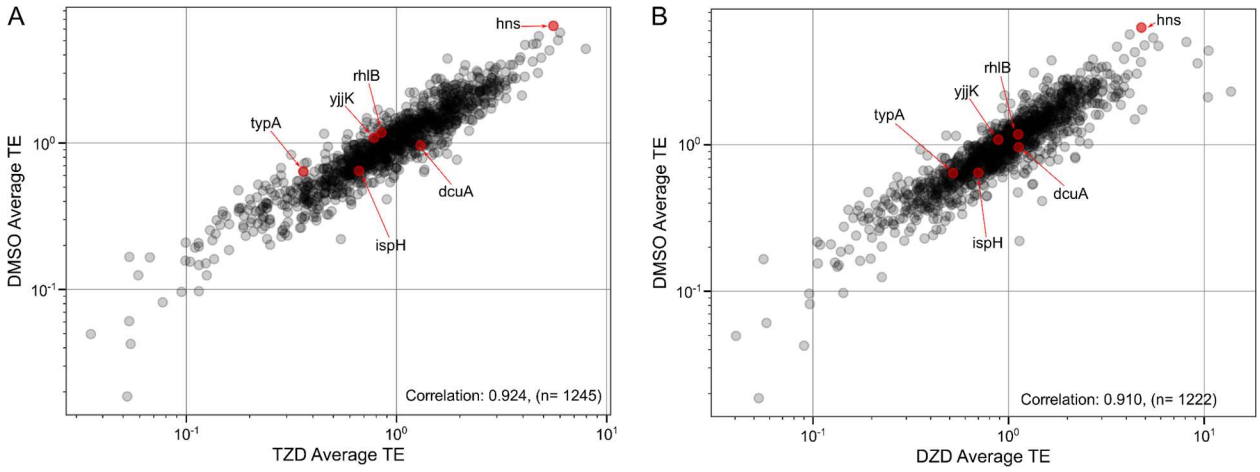

Extended Data Figure 2: Genewise correlation
in translation efficiency between **A)** TZD-treated or **B)** DZD-treated conditions and DMSO control via ribosome profiling. Genes selected for toeprinting analysis are highlighted in red.

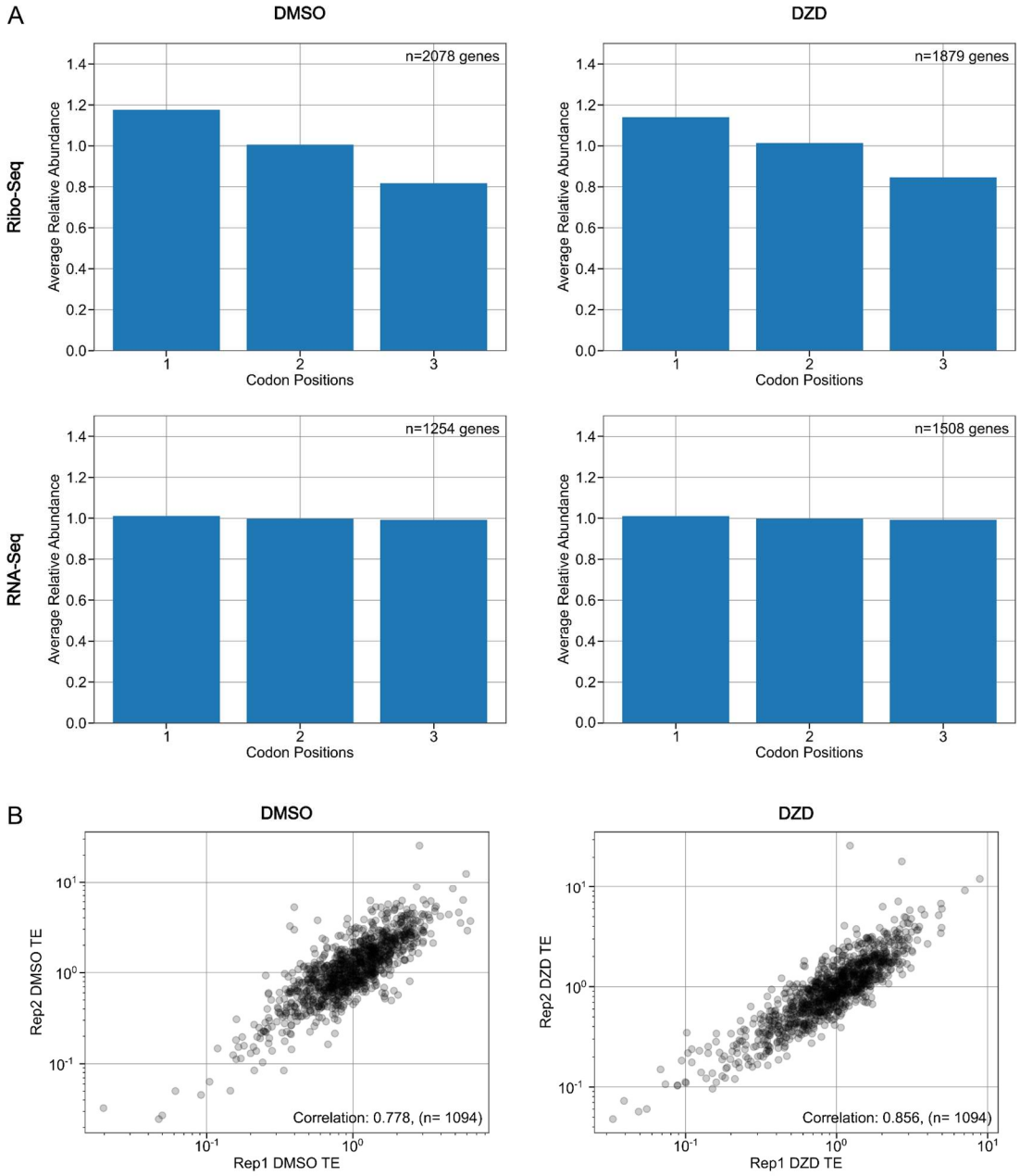

Extended Data Figure 3: Ribosome Profiling Processing After DZD Treatment.
A) Periodicity analysis of profiling data following 2.5 min treatment with DMSO or 10x MIC DZD. Top: Ribosome profiling. Bottom: RNA-seq. **B)** Genewise correlation between replicates. Changes in translation efficiency (RPKM Ribosome profiling/RPKM RNA-seq) for individual genes between experimental replicates following DMSO (left) or DZD (right) treatment.

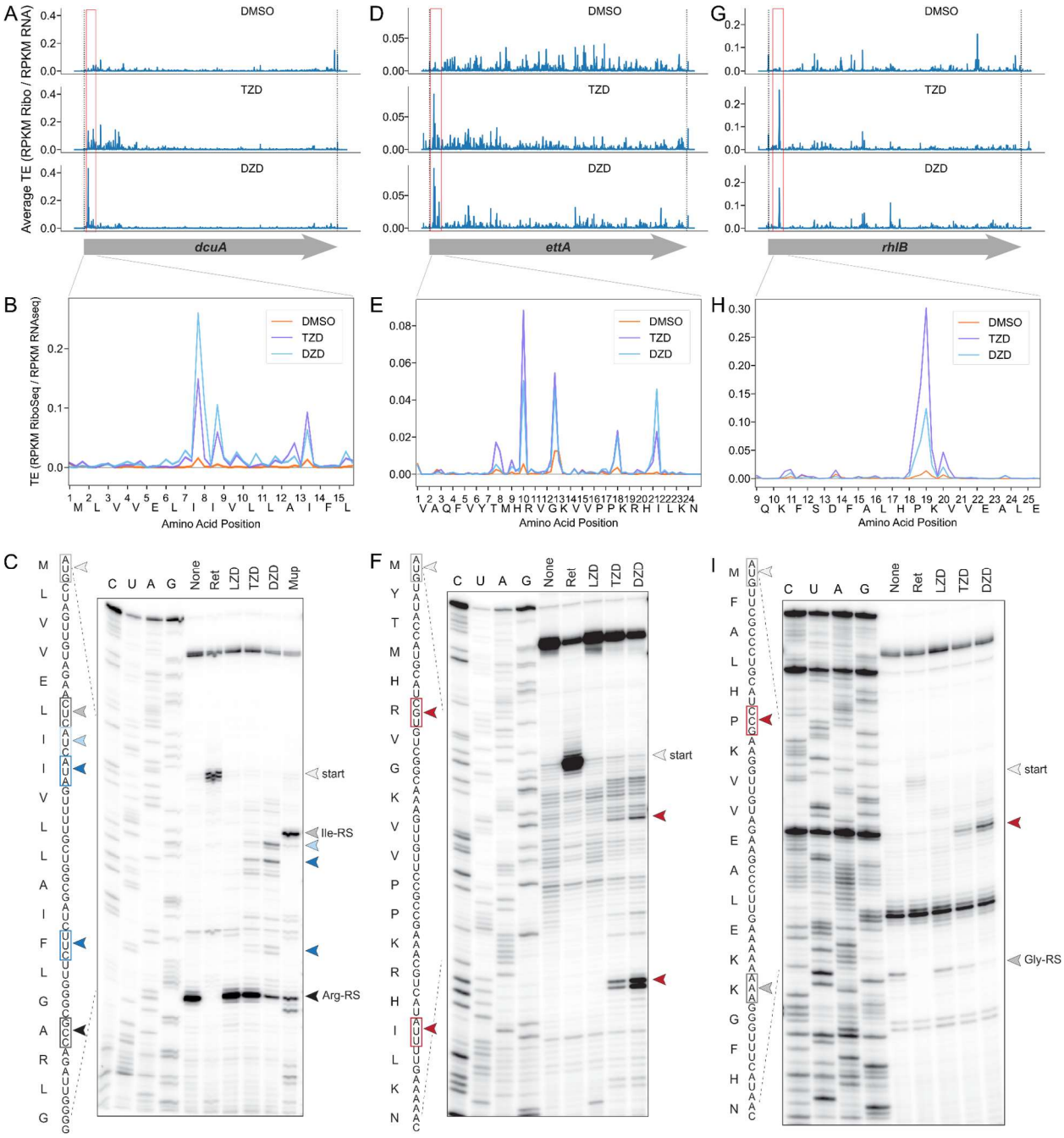

Extended Data Figure 4: Additional validation of Ile(-1) and His(-1) stalling performed on genes *dcuA* (A-C), *ettA* (D-F), and *rhlB* (G-I). **A, D, G)** Ribosome profiling traces across the relevant open reading frames after TZD or DZD treatment. Red boxes highlight prominent drug-induced peaks. **B, E, H)** Zoom into the most prominent stalling peaks for each gene. **C, F, I)** Toeprinting analysis in the presence of LZD, TZD, or DZD. Stalling by retapamulin (Ret) at the start codon is shown in light gray, tRNA-synthetase inhibitors in dark gray or black, Ile(-1) in blue, Leu(-1) in light blue, and His(-1) in red.

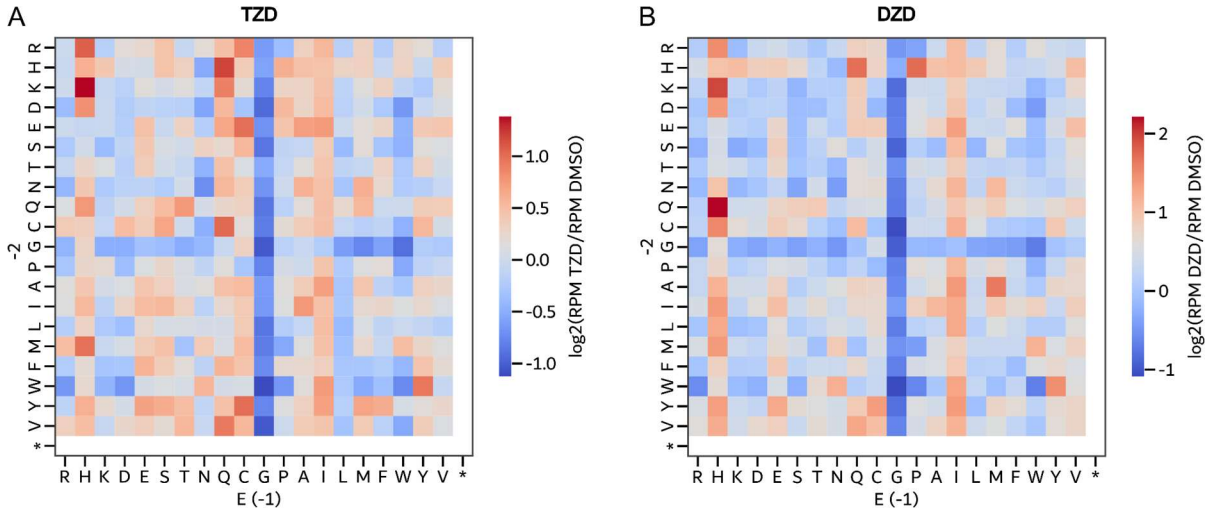

Extended Data Figure 5: Analysis of extended stalling motifs in ribosome profiling data transcriptome-wide
following treatment with **A)** TZD or **B)** DZD. Log2 fold change in average reads per million compared to DMSO control was visualized across all instances of each (-2):(-1) amino acid pairing within the nascent chain in order to evaluate pairwise stalling preferences.

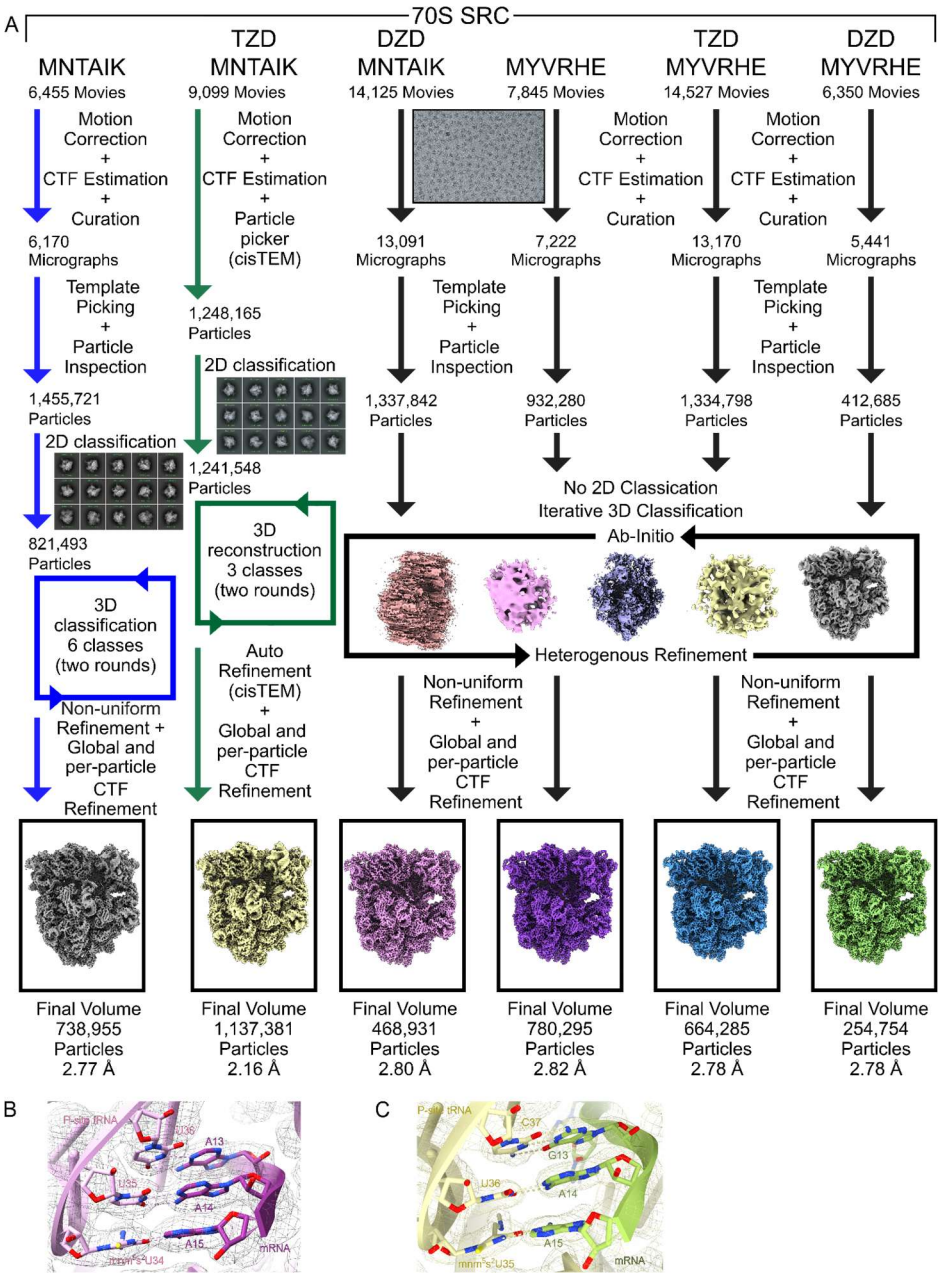

Extended Data Figure 6: Cryo-EM processing pipelines for ribosome reconstructions. **A)** Data processing workflow for generating consensus volumes. Following data acquisition, movies were motion and CTF corrected using MotionCor2[57] and CTFFIND4[58] or CryoSPARC.[59] Next, particles were picked on culled micrographs using template picking from a generated 3D volume, extracted, and then classified using different strategies in either cryoSPARC or cisTEM.[62] Homogeneous particle stacks were re-extracted at the physical pixel size for final refinements. **B)** Density for the decoding center of TZD-MNTAIK SRC at 3.0σ. Nucleotides of P-site tRNA are shown in pink, and those of the mRNA are shown in purple. Dashed lines indicate hydrogen bonds. **C)** Density for the decoding center of TZD-MYVRHE at 6.0σ. Nucleotides of P-site tRNA are shown in yellow, and those of the mRNA are shown in green. Dashed lines indicate hydrogen bonds.

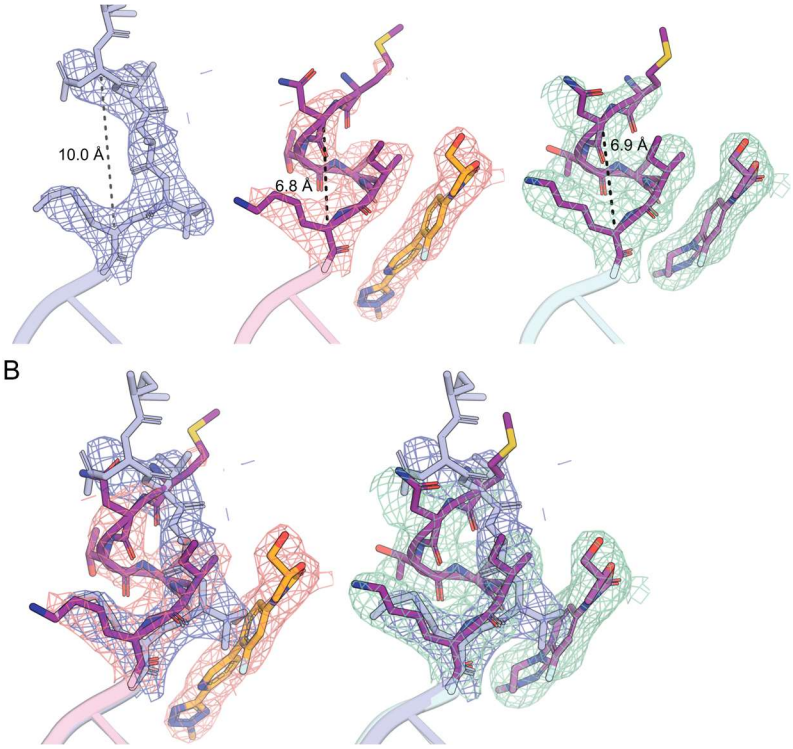

Extended Data Figure 7: Path comparison of nascent peptides in drug-free and drug-bound ribosomes.
A) Measurement of peptide length from Asn(-4) Cα to Lys(0) Cα, shown in black dashed lines, for each complex, including DZD-MNTAIK SRC (peptide in magenta with cyan density). **B)** Overlay of densities for MNTAIK in the TZD-SRC (peptide in magenta with red density) and the drug-free MNTAIK RNC (lavender, blue density).

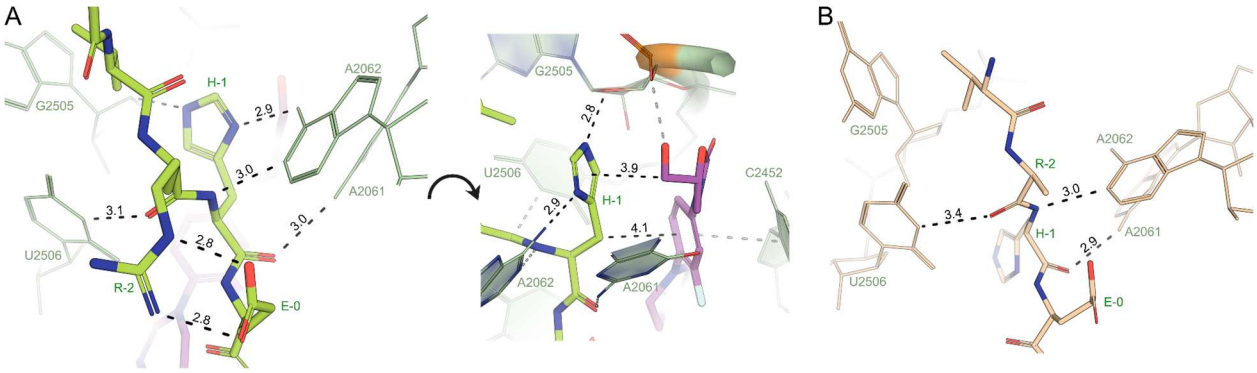

Extended Data Figure 8: Peptide interactions on the DZD-MYVRHE SRC and MYVRHE RNC.
A) Peptide interactions on the DZD-MYVRHE SRC (DZD: purple, peptide: lime, rRNA: green). Distances are denoted in Å. **B)** Peptide interactions on the MYVRHE RNC. Distances are listed in Å.

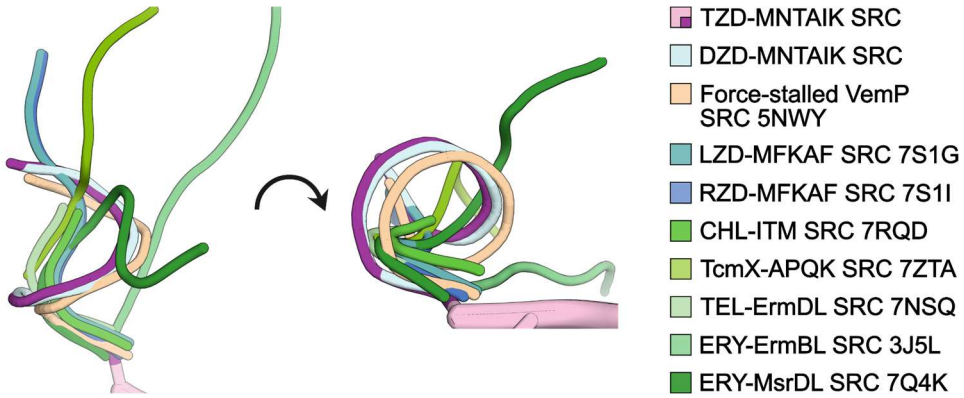

Extended Data Figure 9: Helical peptide path of oxazolidinone-stalled Ile(-1) peptides is unique amongst drug-stalled SRCs.
Comparison of peptide path for TZD-MNTAIK and DZD-MNTAIK SRCs with other drug-stalled peptide complexes (teal: PDB 7S1G; blue: PDB 7S1I; green: PDB 7RQD, 7ZTA, 7NSQ, 3J5L, 7Q4K) and the force-sensitive stalling peptide VemP (beige; PDB 5NWY).

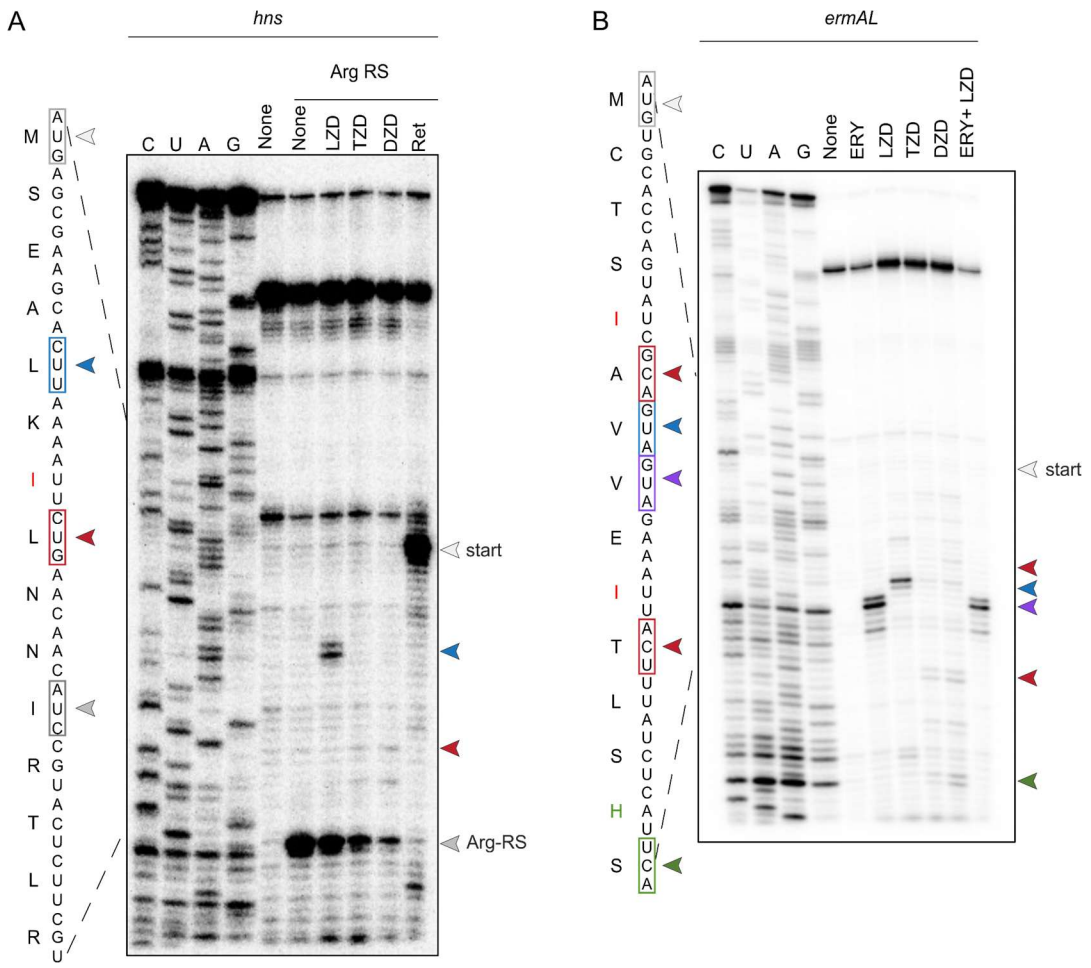

Extended Data Figure 10: Stalling does not occur at all Ile(-1)–containing sites. Toeprinting on mRNA templates derived from *hns* **(A)** or Erm-resistance leader peptide *ermAL* **(B)** in the presence of LZD, TZD, or DZD. Stalling at start codon by retapamulin is shown in light gray, by Arg-RS at Arg(+1) in dark gray, and by LZD at Ala(-1) in blue. **A)** No stalling is observed for the oxazolidinones with Ile(-1) on the *hns* transcript (red). **B)** Little to no stalling is visible at any of the 3 putative TZD and DZD stall sites within *ErmAL* [red: Ile(-1); green: His(-1)]. Erythromycin-mediated stalling (purple) is observed at the canonical site for induction of downstream Erm-resistance genes.[73] All compounds were used at 50 μM.

Supplementary Information

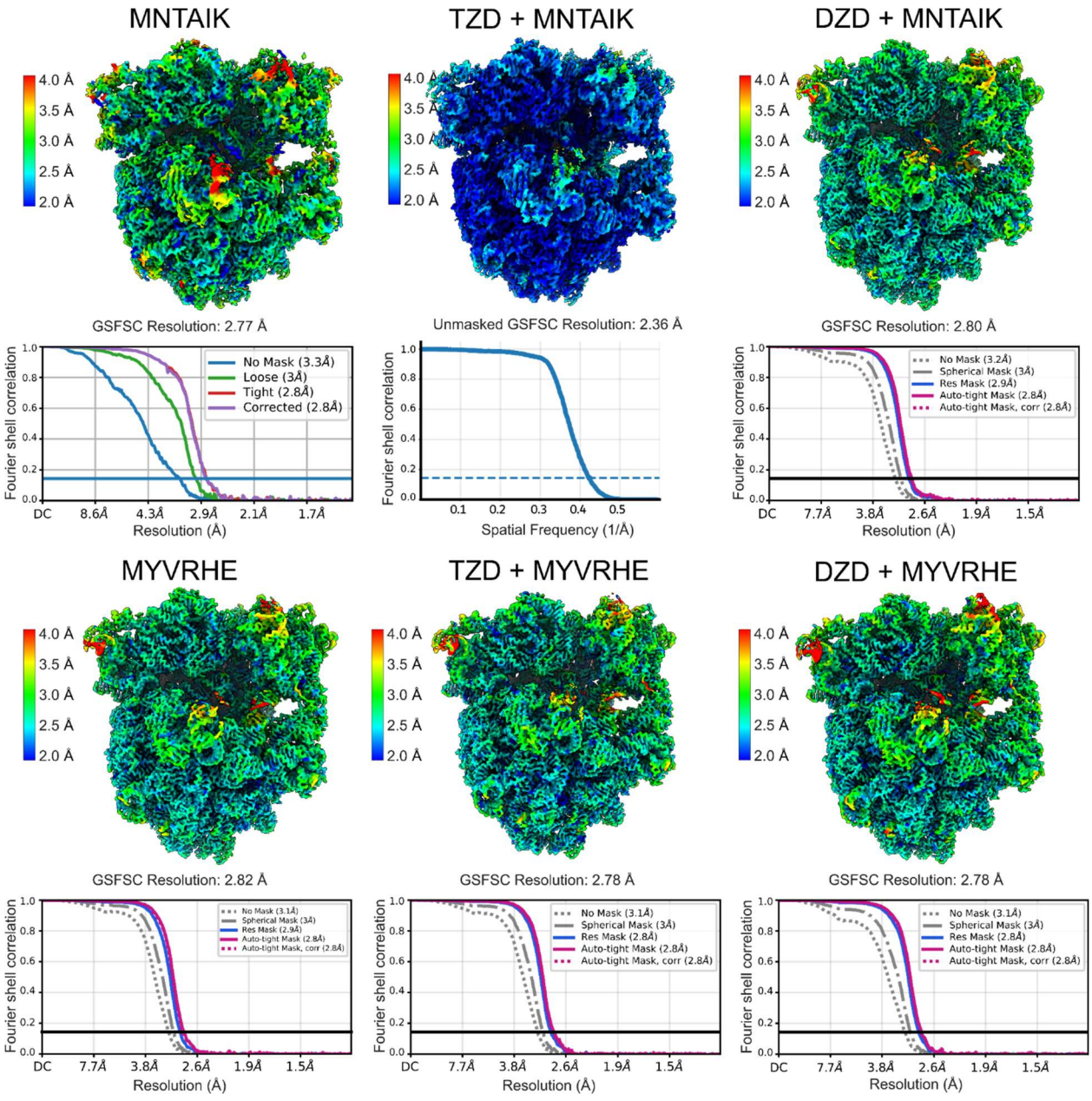

Supplementary Figure 1: FSC curves and local resolution maps for ribosome complexes. The resolution stated is at an FSC = 0.143. All local resolution plots range between 2.0 Å (blue) and 4.0 Å (red).

Supplementary Table 1: Cryo-EM collection, refinement, and validation statistics.

	Ribosome MNTAIK (EMD-75564) (PDB: 10ZE)	Ribosome TZD MNTAIK (EMD-75563) (PDB:10ZD)	Ribosome DZD MNTAIK (EMD-78106) (PDB: 37DY)	Ribosome MYVRHE (EMD-78105) (PDB: 37DX)	Ribosome TZD MYVRHE (EMD-78108) (PDB: 37EA)	Ribosome DZD MYVRHE (EMD-78107) (PDB: 37DZ)
Data collection and processing						
Magnification (kx)	54	105	130	130	130	130
Voltage (kV)	200	300	300	300	300	300
Electron exposure (e–/Å^2)	60	70	15	15	15	15
Movie frames	20	20	20	20	20	20
Defocus range (μm)	-0.6 to -1.5	-0.4 to -1.4	-0.5 to -1.2	-0.5 to -1.2	-0.5 to -1.2	-0.5 to -1.2
Pixel size (Å)	0.73	0.8189	0.64	0.64	0.64	0.64
Symmetry imposed	C1	C1	C1	C1	C1	C1
Initial micrographs (no.)	6,455	9,099	14,125	7,845	14,527	6,350
Final micrographs used (no.)	6,170	9,099	13,091	7,222	13,170	5,441
Initial particle images (no.)	1,455,721	1,248,165	1,337,842	932,280	1,334,798	412,685
Final particle images (no.)	738,955	1,137,381	468,931	780,295	664,285	254,754
Map resolution (Å)	2.77	2.16	2.80	2.82	2.78	2.78
FSC threshold	(0.143)	(0.143)	(0.143)	(0.143)	(0.143)	(0.143)
Map resolution range (Å)	1.8 to 20	1.4 to 26	1.4 to 35	1.4 to 35	1.4 to 35	1.4 to 36
Refinement						
Initial model used (PDB code)	7S1G	7S1G	7S1G	7S1G	7S1G	7S1G
Model resolution (Å)	2.50	2.33	2.79	2.81	2.79	2.78
FSC threshold	(0.143)	(0.143)	(0.143)	(0.143)	(0.143)	(0.143)
Map sharpening *B* factor (Å^2)	80	60	111	117	115	101
Model composition						
Non-hydrogen atoms	145,685	145,406	141,900	141,848	141,919	141,900
Protein Residues	5,672	5,670	5,692	5,689	5,691	5,691
Nucleotide Residues	4,638	4,638	4,522	4,522	4,522	4,522
Ligands	199	199	184	183	184	184
Waters	1538	1224	148	150	167	151
B factors (Å^2)						
Protein	9.80/68.4/33.0	26.4/202/78.0	34.4/208/51.2	36.6/244/52.0	30.4/228/47.9	33.7/238/51.3
Ligand	13.4/73.4/39.7	47.1/128/67.8	27.1/101/43.1	23.9/109/43.2	20.2/96.8/39.9	27.8/104/42.5
Nucleotide	40.2/41.1/40.7	27.8/268/89.9	29.8/357/50.8	27.8/392/51.1	27.9/391/46.5	26.3/421/48.8
Water	8.44/33.8/19.2	47.1/128/67.8	23.0/55.9/40.2	20.9/60.0/41.0	15.9/241/37.9	19.8/62.0/39.6
R.m.s. deviations						
Bond lengths (Å)	0.007 (0)	0.005 (0)	0.005 (0)	0.004 (0)	0.004 (0)	0.004 (0)
Bond angles (°)	0.782 (0)	0.610 (0)	0.995 (0)	0.988 (0)	0.995 (0)	0.966 (0)
Validation						
MolProbity score	1.05	1.80	0.957	1.00	0.99	1.04
Clash score	2.70	5.20	1.66	1.69	1.61	2.22
Poor rotamers (%)	0.02	0.14	0.15	0.09	0.06	0.04
Ramachandran plot						
Favored (%)	98.85	97.07	97.76	97.65	97.60	97.82
Allowed (%)	1.15	2.83	2.24	2.35	2.40	2.18
Disallowed (%)	0	0	0	0	0	0

Supplementary Table 2: Primer Sequences used in this study.

Primer Name	Sequence	Purpose
NV1	GGTTATAATGAATTTTGCTTATTAAC	Toeprinting
FKAFK	GCCCCGGTAAGGAAATAAAAATGTTCAAAGCATTCAAAAACATCATACGTACTCGTACTC	Toeprinting
FKAFK-Rev	GGTTATAATGAATTTTGCTTATTAACCTTGCCTGCGCTTAAAGAGTACGAGTACGTATGATGT	Toeprinting
FWD	ATTAATACGACTCACTATAGGGCAACCTAAAACTTACACACGCCCCGGTAAGGAAATAAAAAT	Toeprinting
T7-IR-fwd	TAATACGACTCACTATAGGGCTTAAGTATAAGGAGGAAAACAT	Toeprinting
IR-rhlB	GTATAAGGAGGAAAACATATGTTCGCCCTGCATCCGAAGG	Toeprinting
NV1-rhlB-rev	GGTTATAATGAATTTTGCTTATTAACCGCCAGCGTCAGCGGAAGGGC	Toeprinting
IR-ettA	GTATAAGGAGGAAAACATATGTATACCATGCATCGTGTCGGC	Toeprinting
NV1-ettA-rev	GGTTATAATGAATTTTGCTTATTAACGACACCAATTTTTGCCCCAG	Toeprinting
IR-ispH	GTATAAGGAGGAAAACATATGTATGTCCGTCACGAAGTGGTAC	Toeprinting
NV1-ispH-rev	GGTTATAATGAATTTTGCTTATTAACGTCCGGTACTTCGCTAATC	Toeprinting
IR-typA	GTATAAGGAGGAAAACATATGAACACCGCTATCAAATGGAA	Toeprinting
NV1-typA-rev	GGTTATAATGAATTTTGCTTATTAACCATGGACATTACACGTTCAAC	Toeprinting
IR-dcuA	GTATAAGGAGGAAAACATATGCTAGTTGTAGAACTCATC	Toeprinting
NV1-dcuA-rev	GGTTATAATGAATTTTGCTTATTAACCAGCACCCCCAATCCGCCTG	Toeprinting
SC-15	rArUrGrUrArCrArCrGrGrArGrUrCrG	RiboSeq size selection
SC-45	rArUrGrUrArCrArCrGrGrArGrUrCrGrArCrCrCrGrCrArArCrGrCrGrArUrGrUrArCrArCrGrGrArGrUrCrGrArCrC	RiboSeq size selection
Universal miRNA cloning linker (NEB S1315S)	5′ rAppCTGTAGGCACCATCAAT–NH2 3′	Ligation linker
Ni-Ni-9	/5Phos/AGATCGGAAGAGCGTCGTGTAGGGAAAGAGTGTAGATCTCGGTGGTCGC/iSp18/CACTCA/iSp18/TTCAGACGTGTGCTCTTCCGATCTATTGATGGTGCCTACAG	Reverse transcription
b-rRNA-1	/5Biosg/TCATCTCCGGGGGTAGAGCACTGTTTCG	rRNA depletion

Primer Name	Sequence	Purpose
b-rRNA-2	/5Biosg/GGCTAAACCATGCACCGAAGCTGCGGCAG	rRNA depletion
b-rRNA-3	/5Biosg/AAGGCTGAGGCGTGATGACGAGGCACT	rRNA depletion
b-rRNA-4	/5Biosg/CGGTGCTGAAGCAACAAATGCCCTGCTT	rRNA depletion
b-rRNA-5	/5Biosg/CTGCTTCCAGGAAAAGCCTCTAAGCATCAGG	rRNA depletion
P5	AATGATACGGCGACCACCGAGATCTACAC	NGS amplification
P7_i23	CAAGCAGAAGACGGCATACGAGATCCACTCGTGACT GGAGTTCAGACGTGTGCTCTTCCG	NGS amplification
P7_i24	CAAGCAGAAGACGGCATACGAGATGCTACCGTGACT GGAGTTCAGACGTGTGCTCTTCCG	NGS amplification
P7_i26	CAAGCAGAAGACGGCATACGAGATGCTCATGTGACT GGAGTTCAGACGTGTGCTCTTCCG	NGS amplification
P7_i27	CAAGCAGAAGACGGCATACGAGATAGGAATGTGACT GGAGTTCAGACGTGTGCTCTTCCG	NGS amplification
P7_i28	CAAGCAGAAGACGGCATACGAGATCTTTTGGTGACT GGAGTTCAGACGTGTGCTCTTCCG	NGS amplification
P7_i31	CAAGCAGAAGACGGCATACGAGATATCGTGGTGACT GGAGTTCAGACGTGTGCTCTTCCG	NGS amplification
P7_i32	CAAGCAGAAGACGGCATACGAGATTGAGTGGTGACT GGAGTTCAGACGTGTGCTCTTCCG	NGS amplification
MNTAIK_R	TTTGATAGCGGTGTTCAT	SRC-rev-short
SD_MNTAIK_R	TTTGATAGCGGTGTTCATTTTTATTTCCTTACCGGGGC GTGTGTAAGTTTTAG	SRC-rev-long
MYVRHE_rev	TTCGTGACGGACATAC	SRC-rev-short
SD_MYVRHE_Rev	TTCGTGACGGACATACATTTTTATTTCCTTACCGGGGC GTGTGTAAGTTTTAG	SRC-rev-long
T7	ATTAATACGACTCACTATAGGG	Toeprinting, SRC-fwd-short
T7_fwd_long	ATTAATACGACTCACTATAGGGCAACCTAAAACTTAC ACACGCCCCG	SRC-fwd-long

Methods

Antibiotics

Oxazolidinones were purchased from Ambeed (tedizolid A139024, delpazolid A194738, linezolid A360550, radezolid A653024).

Ribo-Seq & parallel RNA-seq

Ribosome profiling was performed as described previously,[16,47] with minor modifications. Primer sequences are listed in Supplementary Table 2. *E. coli* BW25113 *ΔacrB* were grown overnight at 200 rpm & 37°C in MOPS EZ Rich media (Teknova M2105). Cultures were diluted 1:200 and grown to OD600 ~ 0.3-0.5. Oxazolidinones, dissolved in DMSO at 50x final concentration, were added to log-phase culture at a final concentration of 10x MIC (20 μg/mL TZD, 80 μg/mL DZD). Equal amounts of DMSO were added to the 'no drug' control cultures (2% DMSO final concentration). Cultures were shaken for 2.5 min, then filtered through a 0.2 μm nitrocellulose membrane (Whatman 7182-009), and the filtrate was rapidly flash-frozen. Cells were mechanically lysed on Qiagen TissueLyser II with 650 μL frozen lysis buffer [20 mM Tris pH 8.0, 10 mM $MgCl_2$, 100 mM NH_4Cl, 5 mM $CaCl_2$, 0.4% TritonX-100, 0.1% NP-40, 100 U/mL RNase-free DNase I (Roche 04716728001), 10 U/mL SUPERase-In RNase Inhibitor (Invitrogen AM2696), antibiotic 10x MIC]. Canisters were pre-chilled in LN_2, and lysis was performed over 5 cycles of 3 min at 15 Hz. Pulverized lysate was thawed and clarified by centrifugation at 20,000 xg for 10 min at 4°C. 12.5 AU clarified lysate (~0.5 mg RNA) was digested for 1 hr at 25°C and 1400 rpm with 750 U MNase (Roche 10107921001), and the reaction was quenched with 5 mM EGTA and placed on ice. Clarified lysate was also aliquoted for RNA-seq. Digested samples were then applied to a 10-50% sucrose gradient (20 mM Tris pH

8.0, 10 mM $MgCl_2$, 100 mM NH_4Cl, 2 mM DTT, 10 U/mL SUPERase-In) and centrifuged at 201,000 xg for 2.5 hr at 4°C. Polysome profiles were obtained using the BioComp Fractionator, and monosome-containing fractions were collected and pooled. Combined monosome samples were purified by hot phenol extraction and 20 µg of sample was resolved by 15% TBE Urea gel (Novex EC6885BOX). Ribosome-protected mRNA fragments 15-45 nt in length (guided by primers SC-15 & SC-45) were excised and eluted from gel (RNA Elution buffer: 300mM NaOAc pH 5.5, 1mM EDTA pH 8.0) for library preparation as described below.

For RNA-seq performed in parallel, an additional 12.5 AU clarified lysate aliquots were thawed and hot-phenol extracted. Small RNA and tRNA were removed from the total RNA via MegaClear Transcription Clean-Up kit (Invitrogen, AM1908), and rRNA was depleted using MicrobExpress Bacterial mRNA Enrichment kit (Ambion, AM1905). Remaining mRNA was fragmented using RNA Fragmentation Reagents (Ambion, AM8740) under stringent conditions (95°C 1 min 45 sec). Fragments 20-100 nt in length were selected and purified from 20 µg sample on 15% TBE Urea gel (Novex EC6885BOX) with RNA Elution buffer and applied to the library preparation pipeline below.

Library preparation

Total size-selected mRNA was dephosphorylated using 10 U T4 polynucleotide kinase (NEB M0201L) at 37°C for 1 h. Dephosphorylated RNA was ligated to 0.4 µL of 50 µM Universal miRNA cloning linker (NEB S1315S) using 200 U of T4 RNA ligase 2 truncated KQ (NEB M0373L) for 3 h at 37°C. Ligated products of appropriate size range (32-62 nt) were isolated from 15% TBE Urea gel (Novex EC6885BOX) and eluted with RNA Elution buffer. RNA was converted to cDNA by reverse transcription with 200 U SuperScript IV RT

(ThermoFisher 180900510) and 1.25 µL of 10 µM primer Ni-Ni-9. RT products were resolved on 10% TBE Urea gel (Novex EC6875BOX) and the appropriate size bands (111-141 nt) were eluted out (DNA Elution buffer: 10 mM Tris pH 8.0, 300 mM NaCl, 1 mM EDTA pH 8.0). Circularization of cDNA was performed using 100 U CircLigase ssDNA ligase (Epicentre CL4115K) at 60°C for 1 h. Ribosomal RNA was removed from ribosome profiling samples by incubating with biotinylated primers b-rRNA-1 through b-rRNA-5 and pulling down with MyOne Streptavidin C1 Dynabeads (Invitrogen 65001) to remove corresponding cDNA. Remaining cDNA was PCR amplified with primer P5 and barcoded P7_index primers to add on NGS handles for 5-9 cycles. Amplified DNA (154-184 bp) was then purified from 10% TBE gel (Novex EC6275BOX) and eluted in DNA elution buffer. NGS-amplified products were evaluated on Agilent Tapestation with D1000 kit (ScreenTape 5067-5582, reagents 5067-5583, ladder 5067-5586), pooled, and submitted for sequencing at the UCSF CAT on NovaSeqX with 100 cycle single end sequencing.

Profiling Data Analysis

All profiling data processing and analysis was performed using custom scripts (github.com/jikleinman/RiboSeq-Code) and referencing previous analysis methods.[15,16,30]

Preprocessing

Raw, demultiplexed reads from next-generation sequencing were trimmed to exclude 3' linkers (CTGTAGGCACCATCAAT) using cutadapt version 4.4.[48] Reads with fewer than 15 or greater than 45 nt were excluded from downstream analysis. Sequences of tRNA, rRNA, and tmRNA were copied from the parent strain genome (CP009273.1[49]) to a new fasta file along with ladder (SC-15 and SC-45) and illumina (P5, P7_iXX) primer sequences. This collated file was

used to exclude the described sequences from downstream analysis via Bowtie[50] alignment with a maximum of 2 errors per alignment. Remaining sequences were then Bowtie aligned to the full parent strain *E. coli* BW25113 genome with a maximum allowable error of 2 nt and a maximum of one alignment location within the genome. Bowtie output files were converted to Wig format by aligning reads to their 3' ends, trimming to remove end mismatches and filtering to exclude resulting reads less than 15 nt long. FastQC[51] was performed at each stage to verify quality.

Metagene Analysis

P-site assignment and periodicity analysis were performed essentially as described previously[15]. Periodicity was measured by averaging reads at every third position within coding sequences (CDS) transcriptome-wide, excluding the first 18 nt of each CDS, and comparing between each of the three nt positions. Low-expression and coverage genes (average reads/position < 0.5 and ≤ 20% nonzero reads) were excluded from this analysis. Genes were further filtered to exclude CDS < 100 nt long for the following metagene analyses. Reads were analyzed around the start and stop codons of open reading frames, and the P-site was assigned at -15 nt from the 3' end of measured reads. Read distribution analysis across ORFs was performed as described previously.[32] Nucleotide positions within genes were divided by full gene length and reads were assigned to the resulting fractional position (rounded to two decimal places). Reads were averaged across all ORFs under analysis and plotted.

Gene-level Analysis

P-site aligned reads with an offset of -15 nt were used for all analyses, and gene-level analyses were performed essentially as described previously.[15] Gene RPKM (reads per kilobase per million) scores were calculated by summing reads over the full ORF and normalizing to gene

length and total sequencing depth of the sample. Ribosome profiling RPKM scores were further normalized to RNA-seq RPKM scores, resulting in a measure of translation efficiency (TE) which was used for correlation analysis. Where indicated, TE for each gene was averaged across two replicates for each experimental condition. Statistical significance of differences in TE for each condition compared to DMSO control was calculated using independent t-tests for each gene with Benjamini-Hochberg FDR correction. Data was filtered to exclude ORFs < 18 nt, with ≤ 20% nonzero reads, and < 0.5 average reads/position, and genes not present in both conditions being analyzed after application of these filters were eliminated from analysis.

Codon-level analysis

Codon analyses were performed following the same filters as the gene-level analyses. Further filters were applied to exclude the terminal 2-10 codons of each CDS and codons with fewer than 5 reads total. Codons not appearing in both conditions being analyzed were removed from consideration. Codon reads were normalized to total gene reads to produce pause scores for each codon, and pause scores were averaged across replicates. Average pause scores were sorted on the basis of log2 fold change compared to DMSO.

pLOGO analysis[52] was performed using the top 1000 stalling codons as foreground and all remaining codons as background, selecting an 11 amino acid window with the P-site codon peak at position 10 [(-9):(+1)]. For transcriptome-wide heat maps, codon RPM (reads per million) was calculated by normalizing codon reads to total sequencing depth. These codon RPM scores were applied at each amino acid in an 11mer window [(-9):(+1)] around the peak, and individual amino acid frequency was calculated at each position by averaging RPM scores across all codons and replicates. Heat maps were plotted as the log2 fold change in averaged RPM

scores compared to DMSO control. Pairwise heatmaps were produced to evaluate the frequency of amino acid pairs at the (-2):(-1) positions. For each potential amino acid pairing, codon RPM scores were averaged across all codons and replicates, and the log2 fold change in averaged pairwise RPM was calculated compared to the DMSO control.

Toeprinting

DNA templates used in the toeprinting experiments were prepared by PCR using AccuPrime DNA Polymerase (Thermo Fisher). The sequences of the primers used are listed in Supplementary Table 2. The *ettA, ispH, typA, dcuA, and rhlB* templates were amplified from *E. coli* genomic DNA using universal primer T7-IR-fwd, and gene-specific primers IR-xxxX and NV1-xxxX-rev, where 'xxxX' represents the name of the corresponding gene. The artificial MFKAFKNIIRTRTL template was generated by a 5-primer PCR using primers T7, NV1, FWD, FKAFK and FKAFK-Rev as described.[13]

Toeprinting reactions were carried out in 5 μL of PURExpress transcription-translation system (New England Biolabs) essentially as described previously.[53] Antibiotics and aminoacyl-synthetase (RS)-inhibitors (mupirocin for Ile-RS or Arg-AMS and Gly-AMS for Arg-RS and Gly-RS, respectively) were added to the final concentration of 50 μM unless otherwise indicated. Following 30 min of translation, reverse transcription was carried out for 10 min using toeprinting primer NV1. cDNA products were separated on 6% sequencing gels. The gels were dried, exposed to a phosphorimager screen, and visualized in a Typhoon phosphorimager (GE Healthcare).

Ribosome Purification

E. coli MRE600 were cultured overnight in LB media at 37°C and 220 rpm, then diluted 1:150 in LB and grown to OD ~0.4-0.5. Cells were harvested by centrifugation at 4°C 4000 rpm for 15 min. Pellets were placed on ice and washed briefly (20 mM Tris pH 7.5, 100 mM NaCl, 10 mM $MgCl_2$), divided in half, and flash frozen. Pellets were gently resuspended on ice in 15 mL Buffer AE (20 mM Hepes-KOH (pH 7.5), 200 mM NH_4Cl, 20 mM $Mg(OAc)_2$, 0.1 mM EDTA, 6 mM β-mercaptoethanol, 10 U/mL SUPERase-In) + 0.1 mM PMSF and filtered through a cell strainer. Filtered cells were lysed by 4 passages through an LM10 Microfluidizer (Microfluidics) at 10,000 psi. PMSF, BME, and SUPERase-In were supplemented to account for added volume. Lysate was incubated with 5 U/mL RQ1 RNase-free DNase (Promega M6101) for 15 min at 4°C, then spun down at 30,000 xg for 30 min and S30 fraction supernatant was collected. Tight-coupled ribosomes were purified from S30 fraction via 4x 32% sucrose cushion prepared in buffer 1E (20 mM Hepes-KOH (pH 7.5), 500 mM NH_4Cl, 20 mM $Mg(OAc)_2$, 0.5 mM EDTA, 6 mM β-mercaptoethanol, 10 U/mL SUPERase-In) via 16-18 hr centrifugation at 100,000 xg (28,000 rpm) in Beckman SW41Ti rotor. After removing supernatant, pellets were recombined by resuspension in 1 mL total buffer AE over ~4 hr with slow rocking at 4°C. Remaining non-resuspended particles were cleared by centrifugation at 4°C for 10 min at 10,000 xg and ~400 pmol loaded onto each of 6x 15-30% sucrose gradients prepared in buffer AE. Gradients were spun at 75,416 xg (21,000 rpm) for 16-18 hr at 4°C in a Beckman SW41Ti rotor. Fractionation was performed using BioComp Gradient Fractionator and monosome fractions were collected and combined. Ribosomes were precipitated at 4°C by slow addition of 30% PEG 20,000 in buffer AE to reach 9% PEG final concentration, then centrifuged at 17,500 xg for 10 min at 4°C to remove supernatant. Ribosomes were resuspended in buffer C (50 mM Hepes-

KOH pH 7.5, 150 mM KOAc, 20 mM $Mg(OAc)_2$, 7 mM BME, 20 U/mL SUPERase-In) to ~13.3-20 pmol/µL by rotating at 4°C overnight and 5 µL aliquots were flash frozen in liquid nitrogen for *in vitro* transcription/translation reactions and structural studies.

Stalled Complex Preparation

Non-stop templates for stalled complex preparation are composed of a T7 promoter for use with NEB PURExpress *in vitro* transcription/translation system, a Shine-Dalgarno sequence, and an ORF sequence containing the putative stall site but lacking a stop codon. Templates were synthesized by 4-primer PCR by combining equal volume of a 100 µM SRC-fwd-short, 10µM SRC-fwd-long, 100µM SRC-rev-short, and 10µM SRC-rev-long for the appropriate ORF sequence (Supplementary Table 2), along with 10mM dNTPs (NEB), and amplifying 30 cycles with T_a = 52°C using Phusion High-Fidelity DNA Polymerase (NEB M0530L). PCR products were purified using MinElute PCR Purification kit (Qiagen 28006).

Stalled complexes were formed for cryo-EM structural studies by *in vitro* transcription/translation. 100 µL reactions composed of PURExpress Δribosome kit (NEB E3313S) with 0.8 U/uL SUPERase-In, 100 ng DNA template, 240 pmol purified MRE600 ribosomes, and 5000 pmol (20x molar excess) oxazolidinone or DMSO to 0.5% were prepared on ice and incubated at 37°C for 1 hr. The reaction was halted by moving to ice, then diluted to 190 µL in ice cold Buffer C and loaded onto a 10-50% sucrose gradient prepared in buffer C. Following centrifugation in a Beckman SW41Ti rotor at 22,000 rpm for 16 hr at 4°C, the gradient was divided into 20 fractions using the BioComp Gradient Fractionator and monosome fractions were collected and combined. Ribosomes were precipitated with PEG 20,000 by slow addition at 4°C to a final concentration of 8% PEG, then spun down at 17,500 xg for 10 min at

4°C. The pellet was gently washed with 500 µL buffer C to remove residual sucrose, then resuspended in buffer C to a final concentration of ~1-3 µM by rotating overnight at 4°C. Resuspended complexes were incubated 1 hr at 4°C with 30x molar excess of the appropriate antibiotic in a final concentration of 0.5% DMSO. This incubation step was omitted for the peptide-only complex. Prior to freezing grids, complexes were filtered through 0.22 µm PVDF filter (Millipore UFC30GV00) by centrifugation at 14,000 xg for 5 min.

Cryo-EM

Cryo-EM sample preparation and data acquisition

The ribosome samples were concentrated to 200 nM or 400 nM for grid preparation. Sample was applied to freshly glow discharged (1 mA, 30 sec) Quantifoil R1.2/1.3 Cu 300 Mesh grids with 2 nm continuous carbon. The sample was incubated for 1 s or 30 s at 4°C on the grid prior to vitrification. Blotting was carried out on a FEI vitrobot Mark IV at 90-100% humidity with a blot time of 5 s or 8 s using Whatman #1 filter paper. Grids were screened for monodisperse ribosome particles and ice quality using an FEI Talos Arctica electron microscope (200 kV). Cryo-EM data was collected on a Titan Krios and Talos Arctica transmission electron microscopes at 300 and 200 kV, respectively using automated acquisition via SerialEM (v4.1).[54–56] Both microscopes were equipped with a Gatan K3 Summit Direct Electron Detector and the Krios also had a Gatan BioQuantum Image Filter (20 eV). All image stacks were collected at the physical pixel size. Pixel sizes, magnifications, micrograph counts, defocus values, and the exposures are reported in Supplementary Table 1.

Cryo-EM image processing

The image stacks for the MNTAIK-only and MNTAIK+TZD datasets were motion corrected and dose-weighted using MotionCor2.[57] The contrast transfer function (CTF) estimation was carried out using CTFFIND4[58] for both the datasets.

For the MNTAIK-only dataset, the structure of a ribosome (PDB ID: 7S1G) was used to generate a reference volume and 2D templates for template picking in CryoSPARC.[59] The particle box size was selected using previously established criteria and subjected to 2D classification.[60,61] After discarding the poor particles, an initial homogeneous refinement was used with per-particle CTF and defocus refinement.[59] Next, two rounds of focused 3D classification were carried out using a mask for the tRNA and the peptide followed by a final round of homogeneous refinement (Extended Data Fig. 6A, Supplementary Table 1, Supplementary Fig. 1).

For MNTAIK+TZD dataset, cisTEM (v1.0.0) was used.[62] We used a particle diameter of 120 Å for particle picking followed by 2D classification and auto refinement with three classes, such that one class was used to exclude the bad particles. The other two classes were then merged into a single class. This was followed by coarse (1000 Å in 10 Å steps) and fine (200 Å in 4 Å steps) CTF refinement and single class auto refinement (Extended Data Fig. 6A, Supplementary Table 1, Supplementary Fig. 1).

For the MNTAIK+DZD, MYVRHE+DZD, MYVRHE+TZD, and MYVRHE-only datasets, movies were imported into CryoSPARC and patch motion correction was performed. All micrographs were outputted at the physical pixel size of 0.64 Å/pixel. Following patch CTF correction, micrograph curation, and template picking, particles were extracted and sent directly

to iterative rounds of 3D classification (skipping all 2D classification). Final particle stacks were passed to non-uniform refinements with global and local CTF refinements to yield the consensus cryo-EM reconstructions which were sharpened using EMReady2[63] (Extended Data Fig. 6A, Supplementary Table 1, Supplementary Fig. 1).

Atomic model building and refinement

Initial atomic coordinates for all structures were derived from the cryo-EM structure of wild-type *Escherichia coli* stalled ribosome with antibiotic linezolid (PDB ID: 7S1G). Each starting model was docked into the corresponding cryo-EM density map via rigid-body fitting in UCSF ChimeraX.[64] To facilitate the accurate modeling of non-protein moieties, ligand stereochemical restraints were generated through the eLBOW module[65] within the Phenix software suite.[66] Structural optimization was achieved through a cyclical process of manual rebuilding and local real-space fitting in Coot,[67] followed by automated global refinement against the experimental density using phenix.real_space_refine.[68] The MNTAIK+DZD, MYVRHE+DZD, MYVRHE+TZD, and MYVRHE-only models were also refined using ISOLDE.[69] To ensure high-fidelity ligand geometry and improve the accuracy of electrostatic interactions, this refinement was further supplemented with force-field-based calculations employing the OPLS3e/VSGB2.1 model.[70] Final structural visualizations and figure rendering were executed in PyMOL (v3.0.2).[71] Maps sharpened using phenix.auto_sharpen program were used for the final density representations for the MNTAIK+TZD and MNTAIK-only datasets while EMReady2 was used for MNTAIK+DZD, MYVRHE+DZD, MYVRHE+TZD, and MYVRHE-only. Model quality was evaluated by MolProbity[72] (Supplementary Table 1).

References

1. Syroegin, E. A., Aleksandrova, E. V. & Polikanov, Y. S. Insights into the ribosome function from the structures of non-arrested ribosome–nascent chain complexes. Nature Chemistry 15, 143–153 (2022).
2. Lin, J., Zhou, D., Steitz, T. A., Polikanov, Y. S. & Gagnon, M. G. Ribosome-Targeting Antibiotics: Modes of Action, Mechanisms of Resistance, and Implications for Drug Design. Annu Rev Biochem 87, 451–478 (2018).
3. Wilson, D. N. Ribosome-targeting antibiotics and mechanisms of bacterial resistance. Nature Reviews Microbiology 12, 35–48 (2013).
4. Drainas, D., Kalpaxis, D. L. & Coutsogeorgopoulos, C. Inhibition of ribosomal peptidyltransferase by chloramphenicol. European Journal of Biochemistry 164, 53–58 (1987).
5. Wilson, D. N. et al. The oxazolidinone antibiotics perturb the ribosomal peptidyl-transferase center and effect tRNA positioning. Proc Natl Acad Sci U S A 105, 13339–13344 (2008).
6. Gamerdinger, M. & Deuerling, E. Macrolides: the plug is out. Cell 151, 469–471 (2012).
7. Davis, A. R., Gohara, D. W. & Yap, M.-N. F. Sequence selectivity of macrolide-induced translational attenuation. Proc Natl Acad Sci U S A 111, 15379–15384 (2014).
8. Kannan, K. et al. The general mode of translation inhibition by macrolide antibiotics. Proceedings of the National Academy of Sciences 111, 15958–15963 (2014).
9. Leroy, E. C., Perry, T. N., Renault, T. T. & Innis, C. A. Tetracenomycin X sequesters peptidyl-tRNA during translation of QK motifs. Nature Chemical Biology 19, 1091–1096 (2023).

10. Marks, J. et al. Context-specific inhibition of translation by ribosomal antibiotics targeting the peptidyl transferase center. Proceedings of the National Academy of Sciences 113, 12150–12155 (2016).

11. Tsai, K. et al. Structural basis for context-specific inhibition of translation by oxazolidinone antibiotics. Nat Struct Mol Biol 29, 162–171 (2022).

12. Syroegin, E. A. et al. Structural basis for the context-specific action of the classic peptidyl transferase inhibitor chloramphenicol. Nature Structural & Molecular Biology 29, 152–161 (2022).

13. Choi, J. et al. Dynamics of the context-specific translation arrest by chloramphenicol and linezolid. Nature Chemical Biology 16, 310–317 (2019).

14. Bibel, B. et al. Context-specific inhibition of mitochondrial ribosomes by phenicol and oxazolidinone antibiotics. Nucleic Acids Res 53, (2025).

15. Mangano, K. et al. Context-based sensing of orthosomycin antibiotics by the translating ribosome. Nat Chem Biol 18, 1277–1286 (2022).

16. Zhang, Y. et al. The context of the ribosome binding site in mRNAs defines specificity of action of kasugamycin, an inhibitor of translation initiation. Proc Natl Acad Sci U S A 119, (2022).

17. Koller, T. O. et al. Paenilamicins are context-specific translocation inhibitors of protein synthesis. Nature Chemical Biology 20, 1691–1700 (2024).

18. Arenz, S. et al. Molecular basis for erythromycin-dependent ribosome stalling during translation of the ErmBL leader peptide. Nat Commun 5, 3501 (2014).

19. Arenz, S. et al. Drug sensing by the ribosome induces translational arrest via active site perturbation. Mol Cell 56, 446–452 (2014).

20. Beckert, B. et al. Structural and mechanistic basis for translation inhibition by macrolide and ketolide antibiotics. Nat Commun 12, 4466 (2021).

21. Syroegin, E. A. et al. Structural insights into context-specific inhibition of bacterial translation by macrolides. Nat Commun 16, 9685 (2025).

22. Fostier, C. R. et al. Regulation of the macrolide resistance ABC-F translation factor MsrD. Nature Communications 14, 3891 (2023).

23. Foti, C., Piperno, A., Scala, A. & Giuffrè, O. Oxazolidinone Antibiotics: Chemical, Biological and Analytical Aspects. Molecules 26, (2021).

24. Barbachyn, M. R. & Ford, C. W. Oxazolidinone Structure–Activity Relationships Leading to Linezolid. Angewandte Chemie International Edition 42, 2010–2023 (2003).

25. Brickner, S. J. et al. Synthesis and antibacterial activity of U-100592 and U-100766, two oxazolidinone antibacterial agents for the potential treatment of multidrug-resistant gram-positive bacterial infections. J Med Chem 39, 673–679 (1996).

26. Im, W. B. et al. Discovery of torezolid as a novel 5-hydroxymethyl-oxazolidinone antibacterial agent. Eur J Med Chem 46, 1027–1039 (2011).

27. Zhou, J. et al. Design at the atomic level: generation of novel hybrid biaryloxazolidinones as promising new antibiotics. Bioorg Med Chem Lett 18, 6179–6183 (2008).

28. Skripkin, E. et al. R chi-01, a new family of oxazolidinones that overcome ribosome-based linezolid resistance. Antimicrob Agents Chemother 52, 3550–3557 (2008).

29. Jeong, J.-W. et al. In vitro and in vivo activities of LCB01-0371, a new oxazolidinone. Antimicrob Agents Chemother 54, 5359–5362 (2010).

30. Mohammad, F., Green, R. & Buskirk, A. R. A systematically-revised ribosome profiling method for bacteria reveals pauses at single-codon resolution. (2019) doi:10.7554/eLife.42591.

31. Schuller, A. P., Wu, C. C., Dever, T. E., Buskirk, A. R. & Green, R. eIF5A Functions Globally in Translation Elongation and Termination. Molecular cell 66, (2017).

32. Diamond, P. D. et al. Context-dependent translation inhibition as a novel oncology therapeutic modality. bioRxiv (2025) doi:10.1101/2025.01.09.632223.

33. Butler, M. S. & Paterson, D. L. Antibiotics in the clinical pipeline in October 2019. J Antibiot (Tokyo) 73, 329–364 (2020).

34. Xiao, Y. & Woods, R. J. Protein–Ligand CH−π Interactions: Structural Informatics, Energy Function Development, and Docking Implementation. Journal of Chemical Theory and Computation (2023) doi:10.1021/acs.jctc.3c00300.

35. Schmeing, T. M., Huang, K. S., Strobel, S. A. & Steitz, T. A. An induced-fit mechanism to promote peptide bond formation and exclude hydrolysis of peptidyl-tRNA. Nature 438, 520–524 (2005).

36. Zhang, J. et al. Mechanisms of ribosome stalling by SecM at multiple elongation steps. Elife 4, (2015).

37. Polikanov, Y. S. et al. Distinct tRNA Accommodation Intermediates Observed on the Ribosome with the Antibiotics Hygromycin A and A201A. Mol Cell 58, 832–844 (2015).

38. Su, T. et al. The force-sensing peptide VemP employs extreme compaction and secondary structure formation to induce ribosomal stalling. Elife 6, (2017).

39. Melnikov, S. et al. Molecular insights into protein synthesis with proline residues. EMBO Rep 17, 1776–1784 (2016).

40. Gersteuer, F. et al. The SecM arrest peptide traps a pre-peptide bond formation state of the ribosome. Nature Communications 15, 2431 (2024).

41. Herrero del Valle, A. et al. Ornithine capture by a translating ribosome controls bacterial polyamine synthesis. Nature Microbiology 5, 554–561 (2020).

42. van der Stel, A.-X. et al. Structural basis for the tryptophan sensitivity of TnaC-mediated ribosome stalling. Nat Commun 12, 5340 (2021).

43. Sohmen, D. et al. Structure of the Bacillus subtilis 70S ribosome reveals the basis for species-specific stalling. Nat Commun 6, 6941 (2015).

44. Vázquez-Laslop, N. & Mankin, A. S. Context-Specific Action of Ribosomal Antibiotics. Annu Rev Microbiol 72, 185–207 (2018).

45. Schwarz, S., Kehrenberg, C., Doublet, B. & Cloeckaert, A. Molecular basis of bacterial resistance to chloramphenicol and florfenicol. FEMS Microbiol Rev 28, 519–542 (2004).

46. Lovett, P. S. Translation attenuation regulation of chloramphenicol resistance in bacteria--a review. Gene 179, 157–162 (1996).

47. Mohammad, F. & Buskirk, A. R. Protocol for Ribosome Profiling in Bacteria. Bio Protoc 9, (2019).

48. Martin, M. Cutadapt removes adapter sequences from high-throughput sequencing reads. EMBnet.journal 17, 10–12 (2011).

49. Grenier, F., Matteau, D., Baby, V. & Rodrigue, S. Complete Genome Sequence of Escherichia coli BW25113. Genome Announc 2, (2014).

50. Langmead, B., Trapnell, C., Pop, M. & Salzberg, S. L. Ultrafast and memory-efficient alignment of short DNA sequences to the human genome. Genome Biol. 10, R25 (2009).

51. Andrews, S. FastQC: a quality control tool for high throughput sequence data. http://www.bioinformatics.babraham.ac.uk/projects/fastqc (2010).

52. O'Shea, J. P. et al. pLogo: a probabilistic approach to visualizing sequence motifs. Nat Methods 10, 1211–1212 (2013).

53. Orelle, C. et al. Identifying the targets of aminoacyl-tRNA synthetase inhibitors by primer extension inhibition. Nucleic Acids Res 41, e144 (2013).

54. Li, Q. et al. Synthetic group A streptogramin antibiotics that overcome Vat resistance. Nature 586, 145–150 (2020).

55. Cheng, A. et al. High resolution single particle cryo-electron microscopy using beam-image shift. J Struct Biol 204, 270–275 (2018).

56. Mastronarde, D. N. Automated electron microscope tomography using robust prediction of specimen movements. J Struct Biol 152, 36–51 (2005).

57. Zheng, S. Q. et al. MotionCor2: anisotropic correction of beam-induced motion for improved cryo-electron microscopy. Nat Methods 14, 331–332 (2017).

58. Rohou, A. & Grigorieff, N. CTFFIND4: Fast and accurate defocus estimation from electron micrographs. J Struct Biol 192, 216–221 (2015).

59. Punjani, A., Rubinstein, J. L., Fleet, D. J. & Brubaker, M. A. cryoSPARC: algorithms for rapid unsupervised cryo-EM structure determination. Nat Methods 14, 290–296 (2017).

60. Rosenthal, P. B. & Henderson, R. Optimal determination of particle orientation, absolute hand, and contrast loss in single-particle electron cryomicroscopy. J Mol Biol 333, 721–745 (2003).

61. Watson, Z. L. et al. Structure of the bacterial ribosome at 2 Å resolution. Elife 9, (2020).

62. Grant, T., Rohou, A. & Grigorieff, N. cisTEM, user-friendly software for single-particle image processing. Elife 7, (2018).

63. Cao, H. et al. EMReady2: improvement of cryo-EM and cryo-ET maps by local quality-aware deep learning with Mamba. Nat Commun 17, (2026).

64. Meng, E. C. et al. UCSF ChimeraX: Tools for structure building and analysis. Protein Sci 32, e4792 (2023).

65. Moriarty, N. W., Grosse-Kunstleve, R. W. & Adams, P. D. electronic Ligand Builder and Optimization Workbench (eLBOW): a tool for ligand coordinate and restraint generation. Acta Crystallogr D Biol Crystallogr 65, 1074–1080 (2009).

66. Liebschner, D. et al. Macromolecular structure determination using X-rays, neutrons and electrons: recent developments in Phenix. Acta Crystallogr D Struct Biol 75, 861–877 (2019).

67. Emsley, P. & Cowtan, K. Coot: model-building tools for molecular graphics. Acta Crystallogr D Biol Crystallogr 60, 2126–2132 (2004).

68. Adams, P. D. et al. PHENIX: a comprehensive Python-based system for macromolecular structure solution. Acta Crystallogr D Biol Crystallogr 66, 213–221 (2010).

69. Croll, T. I. ISOLDE: a physically realistic environment for model building into low-resolution electron-density maps. Acta Crystallogr D Struct Biol 74, 519–530 (2018).

70. van Zundert, G. C. P., Moriarty, N. W., Sobolev, O. V., Adams, P. D. & Borrelli, K. W. Macromolecular refinement of X-ray and cryoelectron microscopy structures with

Phenix/OPLS3e for improved structure and ligand quality. Structure 29, 913–921.e4 (2021).

71. Schrödinger, LLC. The PyMOL Molecular Graphics System, Version 1.8. Preprint at (2015).

72. Williams, C. J. et al. MolProbity: More and better reference data for improved all-atom structure validation. Protein Sci 27, 293–315 (2018).

73. Ramu, H. et al. Nascent Peptide in the Ribosome Exit Tunnel Affects Functional Properties of the A-Site of the Peptidyl Transferase Center. Molecular Cell 41, 321–330 (2011).

Publishing Agreement

It is the policy of the University to encourage open access and broad distribution of all theses, dissertations, and manuscripts. The Graduate Division will facilitate the distribution of UCSF theses, dissertations, and manuscripts to the UCSF Library for open access and distribution. UCSF will make such theses, dissertations, and manuscripts accessible to the public and will take reasonable steps to preserve these works in perpetuity.

I hereby grant the non-exclusive, perpetual right to The Regents of the University of California to reproduce, publicly display, distribute, preserve, and publish copies of my thesis, dissertation, or manuscript in any form or media, now existing or later derived, including access online for teaching, research, and public service purposes.

DocuSigned by:
9DB090B7CEB64E4...
Author Signature

08/01/2026
Date